Virtual Reduction of Focal Spot Size in Computed Tomography using Collimation

by

D. BOEKE

to obtain the degree of Master of Science
at the Delft University of Technology,
to be defended publicly on January 31st, 2023.

Daily supervisor:	Dr. ir. M. C. Goorden
Thesis committee:	Prof. dr. F. J. Beekman
	Dr. ir. M. C. Goorden
	Dr. ir. D. Lathouwers

January 29, 2023

Abstract

This thesis aimed to validate Beekman's patent on how collimation could virtually reduce the focal spot size of an existing small-animal cone beam Computed Tomography (CT) system to diminish the penumbra effect [1]. The ever-remaining drive to improve the spatial resolution in CT for enhanced image quality introduces the need for small focal spot sizes, as the focal spot size is directly related to the geometric unsharpness in the image. Therefore, a collimation method was proposed to virtually reduce the focal spot of existing systems as an alternative to fully replace the current X-ray tube.

A collimator was designed, consisting of numerous tiny hexagonal-shaped holes focused at the center of the focal spot. Theoretical derivations were formulated for its dimensions, and the collimator's efficacy was validated using Monte Carlo simulations. It was concluded that it is theoretically achievable to use collimation to virtually reduce the focal spot size to an arbitrarily chosen smaller virtual focal spot for existing CT systems, significantly reducing the penumbra effect, without requiring any integral changes to the X-ray tube. However, the collimator's practical suitability and manufacturing feasibility were problematic due to its significantly low collimator sensitivity and exceptionally tiny dimensions.

Future work could build on this thesis by obtaining reconstructions from multiple projections of the virtual focal spot to quantitatively assess their theoretically improved spatial resolution. The quantitative confirmation could further establish the theoretical effectiveness of focal spot collimation for future work to enhance reconstructions to uncover valuable information previously hidden.

Contents

1 | Introduction

1.1 Spatial Resolution in Computed Tomography

The principle of Computed Tomography (CT) has been around for over half a decade, and its introduction has drastically revolutionized development in both research and healthcare [2]. It has provided the possibility to obtain a non-invasive visualization of the inside of a subject by the use of X-ray radiation, which has proven to be incredibly valuable for many applications. This includes early medical diagnosis, preliminary tests in animal research, archaeological discoveries, evaluation of the micro-structure of building materials, and many more [3, 4].

Due to this high applicability of CT, there is an ever-remaining technological drive to keep improving the spatial resolution for improved image quality, confirmed by the many publications on spatial resolution. Further improvement of spatial resolution will inherently help increase the correctness of the conclusions in existing applications and could pave the way for even more applications of CT on an even smaller scale. Therefore, improving the spatial resolution of CT could benefit a wide range of fields in our modern world, positively affecting us all. For the research field in particular, improving the spatial resolution of small-animal CT could lead to new invaluable insights by uncovering previously imperceptible details. These small-animal CT scanners were the focus of this work.

The spatial resolution of a CT system is logically closely related to the total geometric unsharpness of a scanned subject U_t. Yester and Barnes have shown that U_t can be derived from a CT scanner geometry as:

$$U_t = \frac{\sqrt{W_{\mathrm{pixel}}^2 + \left[W_{\mathrm{FS}}\left(M-1\right)\right]^2}}{M} \tag{1}$$

where M is the magnification factor of the projection, which is determined by the distances to the subject from the focal spot and the detector, W_{pixel} is the detector's pixel width, and W_{FS} is the focal spot width [5]. Small-animal CT often employs relatively large M to visualize small details inside the subject. When approaching the limit $M \to \infty$, equation 1 shows that the W_{FS}-term dominates the unsharpness present in the reconstruction; therefore, the focal spot width is considered the main limiting factor of the achievable spatial resolution in small-animal CT.

1.2 Penumbra Effect

In previous work by Wang and Fleischmann, the finite size of the focal spot is confirmed as one of the main factors affecting spatial resolution in CT [6]. This limiting

factor manifests itself as the penumbra effect. The ideal image reconstruction assumes that the measured radiation is emitted from a point source. However, the focal spot has a finite size, giving rise to a geometric inaccuracy in the reconstruction due to the distance between the theoretical point source and the precise practical origin of the measured radiation. The inaccuracy induces geometric unsharpness to the reconstruction, called the penumbra. Figure 1 depicts an illustrative example of the penumbra effect. It shows that reducing the focal spot size will decrease the total geometric unsharpness U_t and provide more accurate images.
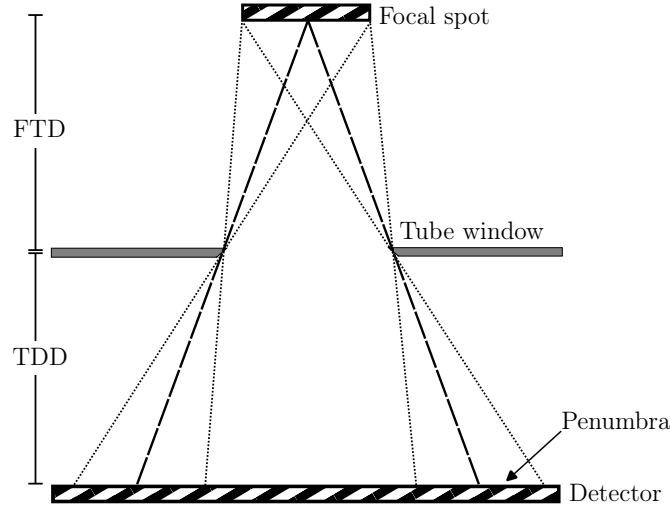
Figure 1. Diagram illustrating the geometric unsharpness of the projection due to the penumbra effect, with *FTD* the focus-tube distance and *TDD* the tube-detector distance, which determine the magnification factor M. The focal spot width and the magnification factor determine the size of the penumbra.

1.3   Reduction of Focal Spot Size

While there is a considerable amount of research on influencing the other factors described by Wang and Fleischmann, there seems to be a gap in the literature regarding the reduction of the focal spot size besides an alternative X-ray tube setup [6]. As replacing the X-ray tube is usually costly or impractical, finding alternative methods to reduce the focal spot size of existing CT systems is an exciting research direction to help further improve spatial resolution [1]. Some focal spot reduction methods have been published, such as deconvolutions or variably narrowing the electron beam. However, these methods either focus on mitigating the penumbra's consequences rather than preventing them or are virtually impossible to implement in existing systems.

A patent by Beekman was published in 2021, in which Beekman conceived the concept of using collimation to virtually reduce the focal spot size of X-ray sources [1]. Beekman proposed placing a collimator with numerous passages near the X-ray tube and having the passages' central directions originate from the same focal point in the focal spot. Based on the passages' width and length, the apparent origin of

each passage will be a 'smeared out' focal point, the virtual focal spot. The concept is visualized in figure 2.
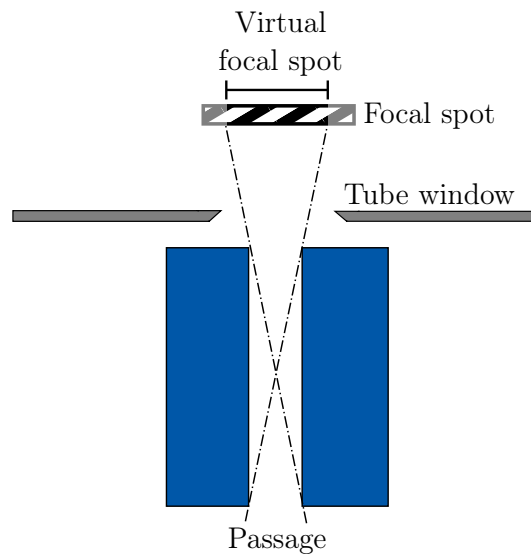
Figure 2. Simplified diagram of a single passage showing the concept of the collimator as proposed by Beekman [1]. The introduction of the passage filters out the emissions from the focal spot's grayed-out sections. Therefore, the detector only notices the virtual focal spot.

Theoretically, when the dimensions of this collimator are chosen appropriately, the virtual focal spot perceived by the detector may be substantially smaller than the X-ray tube's actual focal spot [1]. Such a collimation method would lessen the penumbra effect by reducing the focal spot width and could be smoothly implemented in an existing system outside the X-ray tube. Therefore, further exploration of Beekman's collimation method introduces the research goal of this work.

1.4 Research Goal and Plan

This thesis sought to validate Beekman's patent on how collimation could virtually reduce the focal spot size of an existing small-animal cone beam CT system to diminish the penumbra effect. For this purpose, a collimator was designed based on several design criteria and an initial given exemplary small-animal cone beam CT system. Monte Carlo simulations were conducted to test the collimator's efficacy and to evaluate potentially raised issues, such as the introduction of extra scatter.

The following Literature section will provide a detailed review of the theory and methods related to the research question represented in the current literature. The Methods section will describe the followed design process of the collimator and explain its validation testing with Monte Carlo simulations. The designed collimator will be presented in the Results section, along with the simulation's outcomes. Finally, the Discussion will debate the design and results' positives and shortcomings, followed by the Conclusion of the thesis.

2 | Literature

The following section outlines the current theory and methods related to the research goal in the present literature. The outline started with the fundamentals of CT, followed by literature on the influence of the focal spot on the system performance, and current ways to reduce the focal spot size, and ended with papers on collimator theory.

2.1 Basics of Computed Tomography

2.1.1 X-ray production

CT relies on high-energy electromagnetic radiation, referred to as X-rays, to penetrate the human body. The production of this radiation occurs inside the X-ray tube of the imaging system, which converts electrical energy into a combination of X-ray radiation and heat [7, 8, 9]. The contents of the X-ray tube can be simplified into three principal working components: the filament, the anode, and the cathode [10]. The schematic setup of these components can be seen below in figure 3.
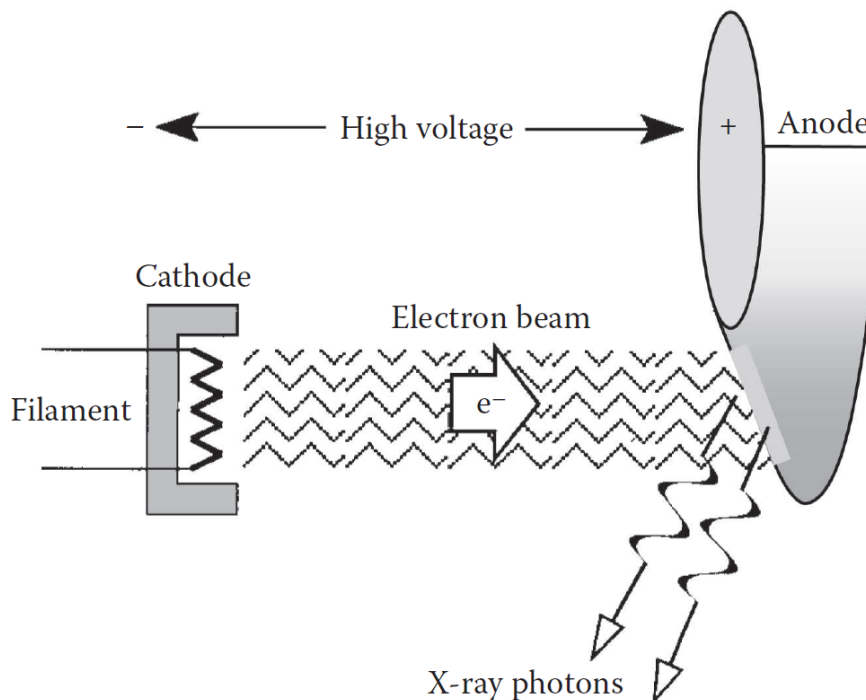
Figure 3. Schematic of the setup of the main components in the X-ray tube within a vacuum [7].

By applying a variable tube voltage, the cathode and the anode are negatively

and positively charged electrodes, respectively, creating a high electrical potential between the two. A variable electrical current is then supplied to the filament, which is a tightly coiled wire. The tube current causes the filament to heat up, eventually leading to the thermionic emission of electrons from the wire [11, 12]. By increasing the current, more electrons are freed from the filament. The high voltage potential accelerates these free electrons toward the target (anode). Upon reaching the target, the electrons will interact with the target atoms, converting their kinetic energy into other forms of energy.

Only 1% of the released energy occurs as X-ray radiation, while the remaining 99% is lost as heat [9]. Heat is produced due to electrostatic repulsion between the incoming electrons and the many electrons bound to the target atoms, which releases a large quantity of low energetic electromagnetic radiation - most commonly in the infrared range of the spectrum [7]. X-ray radiation comprises two classes of radiation: characteristic radiation and bremsstrahlung [7]. Characteristic radiation is primarily emitted from the target atom when an incoming electron with sufficient kinetic energy ionizes a target electron after collision. An electron bound to an outer orbital will drop to the hole left by the ionization while releasing electromagnetic radiation with discrete energy determined by the difference between the ionization energy of the two respective orbitals. Since each material has specific ionization energies, the emitted characteristic radiation is related to the chosen target material [13]. Bremsstrahlung is caused by the deflection of the incoming electron when it passes the positively charged nuclei of the target atoms. The change in momentum of the electron results in the emission of electromagnetic radiation with energy directly related to how close the electron passes the nucleus [7]. Therefore, unlike the characteristic radiation, bremsstrahlung results in a radiation output with a continuous energy spectrum. The radiation can only effectively exit the tube through the tube window as the rest of the tube is shielded. The window mainly determines the radiation beam shape and size. Figure 4 visualizes an example of an energy spectrum of the output.
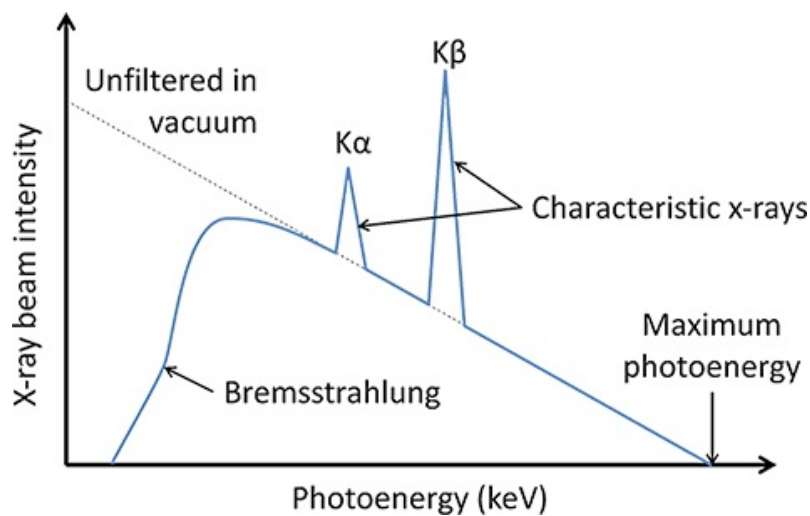
Figure 4. Example of a radiation energy spectrum emitted from a tungsten target [14].

The influence of using different materials for the X-ray tube components has been studied in-depth in previous work [15, 16, 17]. Due to its high atomic number, high density, and low cost, lead is most commonly used to shield the X-ray tube to prevent radiation leakage from the tube [18]. In practice, the cathode-filament composite is primarily made of tungsten, considering its high melting point and favorable thermionic work function [16, 19, 20]. The choice of anode material significantly influences the X-ray tube output since the material determines the characteristic radiation. An important consideration is the large quantity of heat produced at the target. Modern imaging systems often use disk-shaped rotary anodes to dissipate the generated heat more efficiently [21]. The anode is typically either made of tungsten or a tungsten-rhenium alloy, again due to the high melting points, with a low percentage of rhenium being added to improve the target's durability [22]. Occasionally, molybdenum or rhodium are used as target materials, which both emit lower energetic characteristic radiation compared to the characteristic radiation of tungsten. The lower energetic radiation can be especially beneficial for the application of mammography since the breast tissue that needs to be penetrated is significantly less dense than bone tissue [23].

2.1.2 Image reconstruction in Computed Tomography

The emitted X-ray radiation enables the visualization of the inside of a subject of interest. When traversing the subject, the radiation beam gets attenuated based on the density of the matter traversed and the radiation energy, after which the system detector measures the attenuated beam. In modern digital systems, these are typically scintillation detectors, which occur in many different configurations [24, 25, 26]. The measured attenuated X-ray radiation along each line between the X-ray source and the detector provides a superimposed projection of the insides of the subject, like in conventional radiography [27]. CT captures these projections from multiple viewing angles and positions to reconstruct a three-dimensional image of the subject and its center. Therefore, the reconstruction is a three-dimensional map of the subject's linear attenuation coefficient μ. Several reconstruction methods can be used for this purpose, such as filtered back-projection and iterative methods. The suitability of each reconstruction method depends on system factors like the detector configuration, the beam shape, and the available computational power [28, 29]. This three-dimensional representation can provide crucial information to physicians lacking in the superimposed two-dimensional images from conventional radiography.

2.1.3 System performance characteristics

Certain performance features characterize the functioning of each CT system since these features heavily depend on system-specific parameters and hardware configurations [30]. A subset of these system characteristics will be explained further below.

Spatial resolution refers to the ability to differentiate between small, nearby, separated structures and is a crucial characteristic of evaluating the reconstruction's veracity [31]. The spatial resolution can be obtained by various methods, most commonly using line pairs or the modulation transfer function (MTF) [32, 33]. The

spatial resolution is affected by a large number of factors [34]. For instance, Kwan et al. evaluated the influence of several cone-beam parameters on the spatial resolution by computing MTFs as a function of cone angle, the radial distance from the axis of rotation, the size of the reconstruction matrix, the back-projection filter used, and the number of projections acquired for the reconstruction [35]. They showed that while differing cone angle and reconstruction matrix size had little effect on the MTF, change in the other examined factors affected the spatial resolution significantly [35]. Geometrical parameters - such as imaging distances, the tube's focal spot size, and the specific detector dimensions and pixel size - also directly relate to the achievable spatial resolution [7]. Since a high spatial resolution offers more detailed information for interpreters of the reconstructed images, different methods to improve the spatial resolution are invariably considered. Currently, medical CT typically provides spatial resolutions in the range of 0.5 to 1 mm [36]. Micro-CT can offer resolutions in the 2 to 150 µm range, while nano-CT reported achievable resolutions of around 0.5 µm [37, 38].

Contrast resolution is defined as the ability to distinguish between slight differences in pixel intensity in the reconstruction of adjacent image regions with similar X-ray attenuation [39]. When these intensity differences are considerably low, image noise can start to make it particularly difficult to make distinctions due to the noise degrading the image [40, 41]. Image noise, often quantified as the standard deviation of the pixel values in a certain assumed homogeneous image region of interest (ROI), is inevitably present in CT reconstructions considering the statistical nature of X-ray production and electrical noise coming from the measurement at the detector [42]. The contrast-to-noise ratio (CNR) is frequently used to quantify the contrast resolution and to assess the image quality [43]. A previous study done by Cohnen et al. quantitatively showed that the amount of noise is inversely linear with the subject's surface dose [44]. This inherently means that an increase in tube current and exposure time will benefit the contrast resolution at the cost of the subject receiving a higher dose. Multiple authors have evaluated the trade-off between these two perspectives in the past twenty years, and it remains an important balance to maintain [45, 46].

2.2 Influence of the Focal Spot

The focal spot of the X-ray tube is the area of the anode that is hit by the free electrons from the filament and from where the X-ray radiation is emitted [47]. The area is determined by the free electron beam, which is controlled by a shallow depression in the cathode surface that acts as a focusing cup. The negatively charged focusing cup counteracts the spread between the free electrons due to their electrostatic repulsion, focusing the electron beam in a specific shape and size onto the anode [48]. The choice for the size of this area has two conflicting constraints: to spread the previously discussed generated heat, the focal spot should be enlarged as much as possible, while to achieve sharper image details, the focal spot size should be minimized [47]. This contradiction is partially resolved by the line focus principle, which is illustrated in figure 5 below [49, 50].
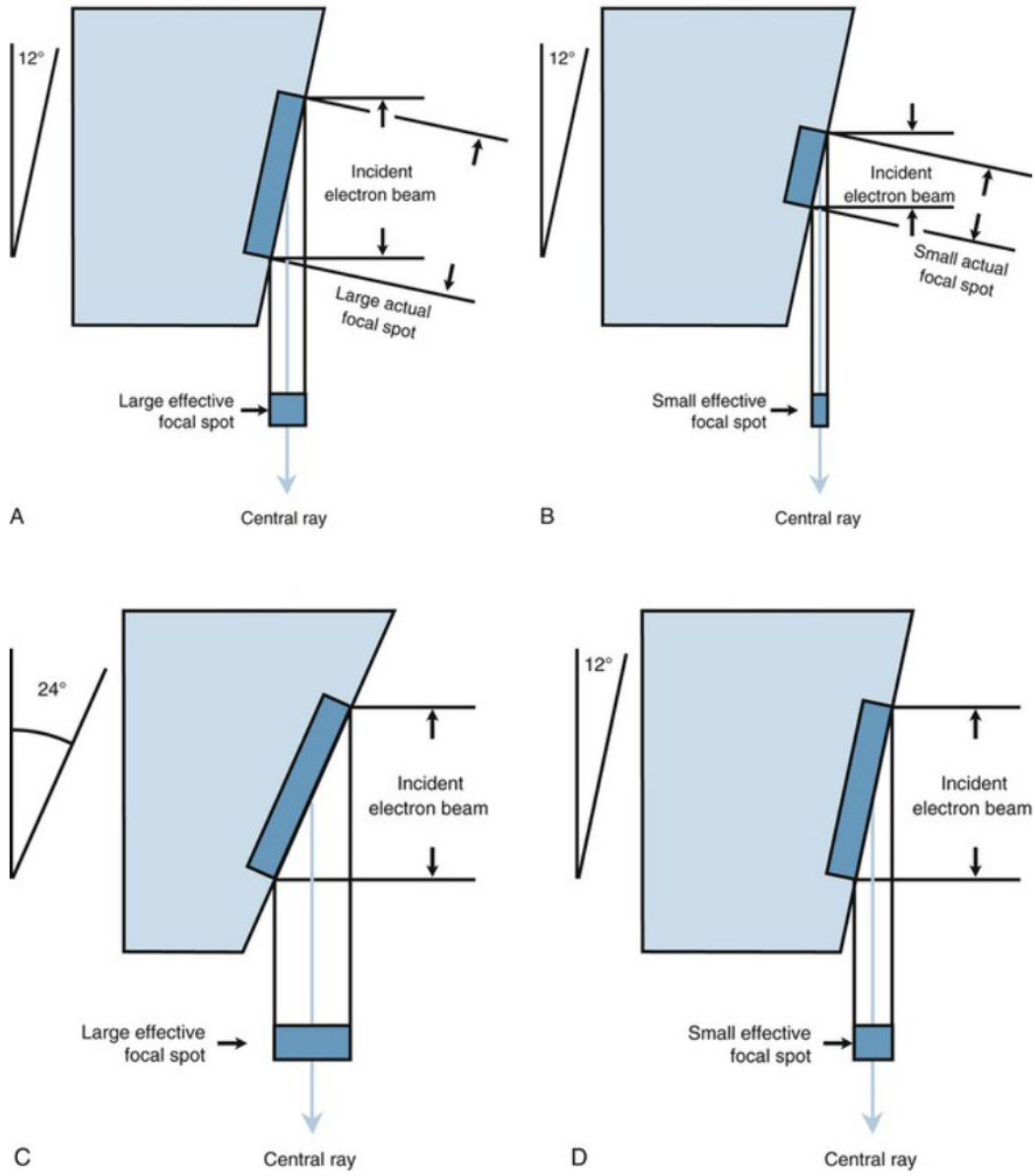
Figure 5. Overview of the line focus principle in different scenarios: between a) and b), the electron beam width is decreased, while between c) and d), the anode angle is decreased. Both decrease the effective focal spot size [50].

The incident electron beam is targeted at an angled anode to increase the actual focal spot's area to help heat dissipation. However, when looking along the central ray of the X-ray output, the effective focal spot size appears to be significantly smaller. The actual and effective focal spot width are related by the following simple equation [50]:

$$W_{\mathrm{FS}} = W_{\mathrm{actual}} \sin \theta \tag{2}$$

where W_{actual} and W_{FS} are the actual and effective focal spot widths, respectively, and θ represents the anode angle as depicted in figure 5. This relation is key in the

design decision between proper heat dissipation and minimizing the effective focal spot size.

The effective focal spot should ideally act as a point source to allow for precise tracking of the path traversed by the non-attenuated photons. However, in practice, the effective focal spot has a finite size, emitting radiation in all directions from its entire area [51]. As the traversed path from the finite focal spot cannot be precisely predicted, it introduces geometrical unsharpness in the reconstruction, called the penumbra, and is illustrated in figure 6 below [7]. The penumbra has a negative effect on spatial resolution.
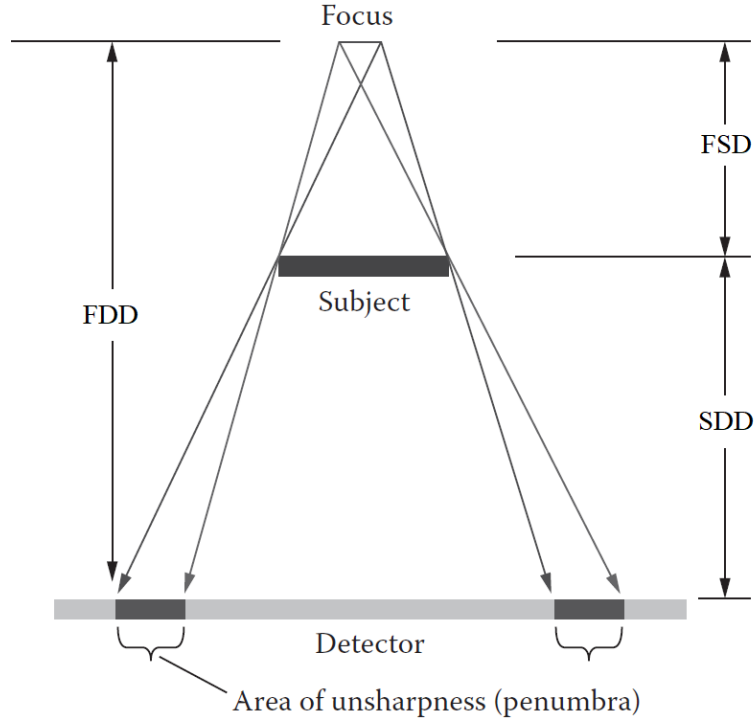
Figure 6. Diagram showing the penumbra on the detector. The size of the penumbra is determined by the focus width and the distances between focus, subject, and detector [7].

The penumbra is affected by a number of factors: the effective focal spot width (W_{FS}), the focus-detector distance (FDD), the focus-subject distance (FSD), and the subject-detector distance (SDD) [7]. From figure 6, the penumbra width (W_{pen}) can be deducted by using similar triangles:

$$W_{\mathrm{pen}} = W_{\mathrm{FS}} \frac{SDD}{FSD} = W_{\mathrm{FS}} \frac{SDD}{FDD - SDD} = W_{\mathrm{FS}} \frac{1}{\frac{FDD}{SDD} - 1} \tag{3}$$

To minimize the penumbra, it is evident that W_{FS} should be minimized while maximizing the ratio of FDD and SDD. The latter can be realized by increasing the FDD while placing the subject as close as possible to the detector to decrease the

9

SDD. However, this is troublesome in situations where the magnification of a subject is desired. The magnification factor M of the subject image is determined by the ratio of FDD and FSD:

$$M = \frac{FDD}{FSD} = \frac{FDD}{FDD - SDD} = \frac{1}{1 - \frac{SDD}{FDD}} \tag{4}$$

To increase magnification, the ratio between FDD and SDD needs to decrease by placing the subject closer to the tube. Magnification can be helpful to enlarge the fine details of a subject to maximize the obtainable image information and to ensure that the detector resolution does not dominate the system's spatial resolution, as can be deduced from equation 1 [52]. Therefore, magnification can be particularly beneficial when imaging small detailed subjects, such as in small-animal imaging. Nonetheless, the comparison between equation 3 and equation 4 indicates that the need for magnification implicates increased geometrical unsharpness of the reconstructed image due to the decreased ratio between FDD and SDD. As this ratio between the setup lengths is fixed by the desired magnification, equation 1 and 3 show a reduction of the effective focal spot size is the only remaining option to counteract the enlarged penumbra.

2.2.1 Measurement of effective focal spot

The application's requirements guide the effective focal spot size selection as the spatial resolution strongly correlates with the used size due to the penumbra effect. Medical CT often employs focal spots with nominal effective focal spot widths in the 0.3 to 1.5 mm range to obtain sufficient spatial resolution [53]. Meanwhile, typical micro-CT used for research utilizes nominal widths around 100 µm. On an even smaller scale, Nachtrab et al. reported on a nano-focus X-ray tube with a nominal effective focal spot width of approximately 154 nm [54].

Various methods have been proposed to measure the geometry of the effective focal spot and have been compared in-depth in comparison studies [55, 56, 57, 58]. International organizations have attempted to standardize the focal spot measurements to prevent manufacturers from underestimating their focal spot size. The National Electrical Manufacturers Association (NEMA), based in the United States, has provided standards for focal spot measurement that have been widely accepted [56]. More recently, this has been continued by the International Electrotechnical Commission (IEC), which published multiple versions of their 60336-standard, suggesting the use of a specific split measurement setup for medical devices [59]. However, various other methods are still commonly used in practice.

Pinhole measurement magnifies the focal spot to a degree where it becomes a visible projection. The effective focal spot size can be deducted from the magnified projection using the magnification factor [60]. The pinhole measurement is usually susceptible to misalignment errors and is considered time-consuming due to the long exposure times needed [61].

Star test patterns have also been used in the past to assess the effective focal spot size by looking at the blurring of a star pattern caused by spurious resolution at the zero contrast point [55, 61]. However, this resolution method relies on a uniform focal spot intensity distribution to provide accurate results, regularly rendering this method unsuitable [62].

Slit measurements are similar to the working principle of pinhole measurements, except it isolates one dimension of the focal spot to make it easier to evaluate the length in that direction [63]. Similar to the pinhole method, the slit method is also susceptible to misalignment errors. However, the needed exposure time is shorter due to the increased sensitivity compared to the pinhole. This method is recommended by NEMA's and IEC's previously discussed published standards.

Edge response analysis has been a recently proposed method in the study by Nishiki et al. [64]. They isolated the penumbra influence on the edge response using the optical transfer function to acquire a geometrically magnified edge response and a non-magnified edge response. Finally, the focal spot profile was recovered by the inverse Fourier transform. The method showed excellent agreement with conventional slit measurement results with a reported smaller uncertainty [64].

2.2.2 Factors affecting the focal spot

Besides the previously mentioned direct parameters of electron beam width and anode angle, other factors indirectly affect the focal spot in various ways.

Focal spot blooming is an increase in focal spot size due to an increased tube current or decreased tube voltage [65]. When the tube current increases, the experienced electrostatic repulsion increases by the increase of the amount of present free electrons. If the tube voltage is not adjusted appropriately, the focusing cup cannot fully counteract the electrostatic repulsion, and the electron beam spreads out [6]. The same happens when the tube voltage is decreased, allowing the electrons to spread out over a broader trajectory. Therefore, both of these scenarios have a blooming effect on the focal spot. Grimes et al. studied the consequences of focal spot blooming on the achievable spatial resolution [66]. They concluded that the blooming effect could significantly enlarge the focal spot size and degrade the spatial resolution. The dynamic focal spot shaping technique using a quadruple magnetic field was shown to be effective in stabilizing the blooming effect in an extensive range of tube currents.

The anode heel effect occurs at small anode angles where the X-ray radiation beam is non-uniform in intensity in the anode-cathode direction. The concept of the effect is visualized in figure 7 [50]. Due to the electron beam penetrating the anode to a certain depth before interaction, the emitted X-ray radiation has to traverse the anode material before reaching the tube vacuum. The length of the traversed path through the target depends on the emission angle relative to the anode surface [49]. Therefore, radiation emitted at arbitrary angles with the anode surface experiences more attenuation than the radiation perpendicular to that surface, leading to a relatively lower intensity towards the anode in the anode-cathode direction. This

anode attenuation imposes a limitation on the minimization of the anode angle and, thus, on the achievable minimum effective focal spot.
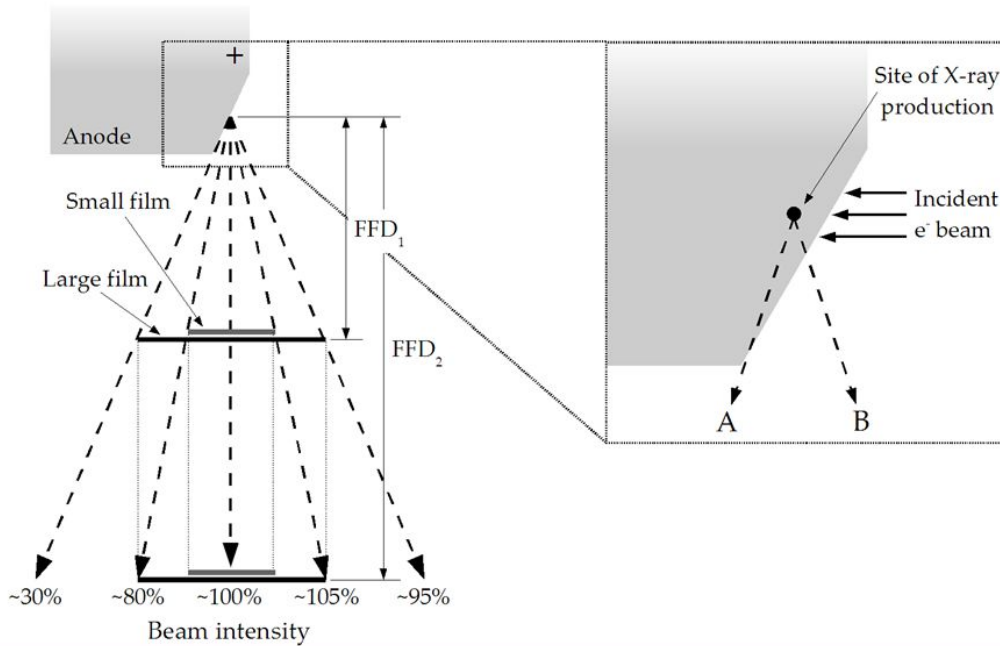
Figure 7. Diagram showing the anode heel effect. The difference between the travel path of A and B inside the anode manifests as a non-uniform intensity distribution [67].

Several methods to compensate for the heel effect have been suggested in studies done in the past. Mori et al. suggested a filter of variable thickness across the direction from anode to cathode to rectify the attenuation deviations among the different ray paths [68]. Other work proposed post-processing solutions to the problem, for example, the study done by do Nascimento et al. [69]. The study shows an intensity correction method based on the theoretical radiation intensity distributions in all directions with a logarithmic distribution parallel to the anode-cathode axis accounting for the heel effect. According to their results, the proposed method eliminated 94% of the presence of the heel effect in the reconstructed images. A recent literature study by Kusk et al. found limited published evidence regarding the impact of the heel effect on the image quality of modern digital radiography [70]. It was suggested that relevant information, such as the used post-processing methods, was insufficient in current heel effect studies to reach absolute conclusions. In some cases, the heel effect is purposely unaccounted for and is used to the physicians' advantage to image a subject with non-uniform density by placing the denser section under the intenser cathode-sided radiation [50].

2.2.3 Impact of effective focal spot size on spatial resolution

The amount of previous research on the direct impact of the effective focal spot size on the reconstruction's visual quality and spatial resolution is limited. A study conducted by Gorham and Brennan used visual grading analysis of anatomical human

CT images acquired using either a fine or broad focal spot to determine its influence in clinical practice [71]. According to their published work, qualitative evaluations by multiple experienced physicians showed no significant statistical difference in image quality between the use of fine or broad focal spots. Therefore, they argue that the assumption that fine focus provides superior image quality in clinical practice needs to be revisited. This conclusion is supported by Kei Ma et al., who looked at the differences in perceptual image quality of human hand phantoms when varying the tube current, tube voltage, and focal spot size [72]. After careful visual evaluation by five diagnostic radiographers, it was concluded that the perceptual image quality did not change depending on the focal spot size. However, these works only evaluated the current clinical difference for medical diagnostic purposes and did not investigate the quantitative improvement of the image resolution.

Recent research done by Mikayama et al. involving ultra-high-resolution CT - which spatial resolution has been reported to be significantly higher than current-generation multi-detector CT - focused on the effect of focal spot size on the error in the measurement of human airway dimensions [73, 74]. The results indicated that using a smaller focal spot led to a statistically significant improvement in the measurement error, almost halving the relative measurement error compared to the larger focal spot. Papadakis and Damilakis came to a similar conclusion, stating that the task-transfer function at 50% degraded with increasing focal spot size [75]. The publication of Nickoloff et al. pointed out the importance of the effective focal spot intensity distribution and geometry instead of only looking at the nominal focal spot width [76]. They found that the use of more centered or uniform intensity distributions with equal diameter geometries increases the resolution over the use of more arbitrary focal spots.

Compared to clinical CT applications, small focal spots are arguably more essential in laboratory applications like small-animal CT due to the need for high spatial resolution [77]. As magnification and micro-scale pixel dimensions are regular in small-animal imaging, the penumbra effect can cause noticeable deviation in the practical spatial resolution compared to the theoretical resolution at higher magnification factors, according to work by Ouandji et al. [77]. Rueckel et al. underwrite the importance of magnification. While the detector and display resolutions are commonly the limiting factors at low magnification, the spatial resolution at high magnification factors is primarily limited by the focal spot size [78]. Therefore, the spatial resolution will not further increase due to the penumbra effect after a particular magnification factor is reached.

2.3 Current Methods to Reduce Focal Spot Size

While most modern clinical CT systems offer a dual focal spot set up to offer the choice between the use of a fine or broad focus, these sizes are usually permanently fixed by tube design [79]. When a reduction of effective focal spot size is desired, it usually means entirely replacing the X-ray tube or even the whole system, which can be a costly endeavor [80]. Therefore, there is a need for conducting research into methods to be able to reduce the focal spot of a fixed tube setup. Even though the

amount of available literature is limited, this subsection aims to provide an overview of the current methods and their limitations.

2.3.1 Deconvolution and integral projections

These methods do not physically reduce the effective focal spot size, but they try to achieve a similar effect and are consequently included in this overview.

Last year, research by Hu et al. was published that aimed to reduce the penumbra effect on small-animal cone-beam CT induced by the finite size of the effective focal spot [81]. At first, they derived the effective focal spot intensity map. The intensity map was used to model the blur that this map induces in the reconstructions using the filtered back-projection algorithm. This eventually allowed them to compute appropriate convolution blur kernels in the image domain, which was used to reduce the penumbra effect to improve spatial resolution by deconvolving reconstructed images with the blur kernels. Their results on both noiseless and phantom projections reported a relative increase in a measured spatial resolution, ranging from 12.0 up to 25.7%, at a slight loss of signal-to-noise ratio (SNR) [81].

The mentioned work shows similarities to the approach by Chang et al., published some years prior. The paper proposed Modeling Finite Focal Spot (MFFS): modeling the finite size focal spot as the integral ideal projection of a given point source over the finite focal spot support [82]. The mathematical model is used to find the linear equivalence relationships between virtual focal spot projections and ideal point source projections. The projections from a virtual fine focus spot can then be recovered from the measured projections of a relatively large focal spot by solving the linear problem following the linear equivalence relationships. Regular reconstruction algorithms can be applied using the obtained virtual focal spot projections to reconstruct images with an improved spatial resolution. The spatial resolution was reported to gain up to a 50% improvement based on the choice of parameters, while it did come at the cost of a decreased SNR [82].

These processing methods offer remarkable improvements in spatial resolution but do not physically alter the effective focal spot size. Instead of reducing the experienced penumbra effect, these methods aim to mitigate its consequences. This puts limitations on the degree of improvement that is achievable. In addition, some cases will not allow for introducing these techniques, considering computational shortcomings or the practicality of implementation on existing systems.

2.3.2 Variably narrowing electron beam

As discussed in the previous subsections, the width of the electron beam is one of the direct parameters that affects the focal spot size. The width is passively controlled by the tube voltage and current; however, their values are primarily set to select the radiation energy and intensity, respectively. The exact electron beam width results from the chosen combination of the tube parameters, leading to the focal spot blooming effect. Research involving more precise control of the electron beam width could provide methods to variably reduce the focal spot size as desired.

The work by Grimes et al. has already been briefly discussed in this study [66]. In their study, the used Siemens Vectron had a system in place of electromagnetic quadruple magnets to dynamically adjust the electron beam shape. The effect of the system on the electron beam is shown below in figure 8.
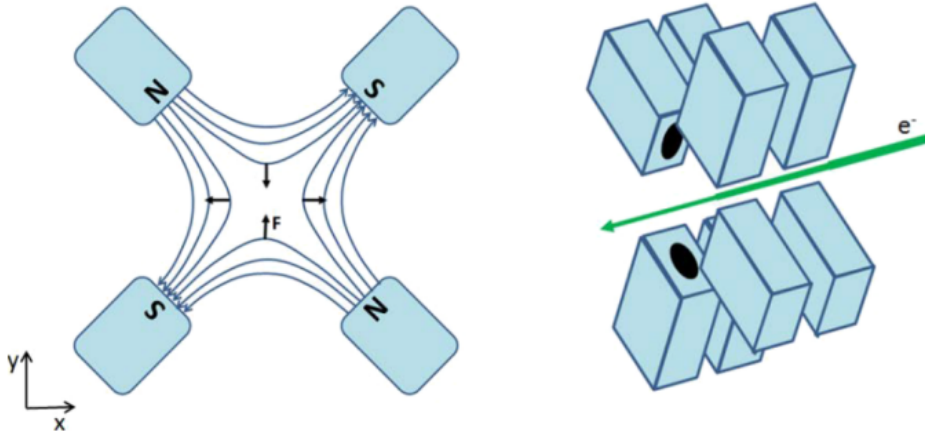
Figure 8. Overview of the dynamic focal spot shaping technique of the Siemens Vectron. On the left are the resulting magnetic field and the direction of the Lorentz-force (F) on electrons (e⁻) moving towards the reader. On the right is a schematic showing a dual quadruple magnet system setup to control the electrons in both x- and y-direction [66].

The resulting magnetic field of the quadruple magnet focuses the electron beam in one direction while defocusing in the perpendicular direction. The strength of the Lorentz force decreases to zero towards the center of the magnet. By precisely combining two sequentially placed quadruple magnets with opposite polarity, the beam is focused at the center of the magnets. The magnetic field strength is determined by the current that is passed through the electromagnets' coils and is dynamically adjusted to the tube voltage to compensate for the blooming effect in the case of the Siemens Vectron [66]. When the coil current could be manually selected, the same system could be used to variably narrow down the electron beam to set the desired focal spot size.

Lillaney et al. looked at the drift of the electron beam in close proximity hybrid X-ray/Magnetic Resonance Imaging systems due to the MRI-induced magnetic fringe field [83]. They proposed the introduction of an external electric field to the X-ray tube by placing two additional electrodes adjacent to the cathode to compensate for this drift effect. The strength of the additional electric field could be manually tuned to match the drift in which they succeeded to a certain degree. The study focused on a one-dimensional drift and corresponding electric field. Nonetheless, the technique could be expandable into two-dimensional beam control with specific adjustments. However, the authors stated the critical design consideration of the dielectric strength inside the vacuum, which puts an important limitation on the spacing of all the different electrodes and the maximum potential between them [83].

The described techniques have promising aspects, especially for future tube designs to get more direct control of the electron beam width. A valid concern is a possible sensitivity to geometry and electrical uncertainties, which will require maximum precision during manufacturing and aligning. Implementing the described electron beam narrowing methods to reduce their focal spot sizes for existing X-ray tubes will be virtually impossible. There will neither be the necessary free space nor the electronic capacity in the tube to incorporate such a technique. That is without considering that the modification cost would likely already approach the costs of replacing the current tube with a superior one, which would also be less effort.

2.3.3 Reduction based on collimation

A patent by Beekman was published in 2021, in which Beekman conceived the concept of using collimation to virtually reduce the focal spot size of X-ray sources [1]. The patent describes the issues of the current small focal spot X-ray sources as being impractical due to their rather bulky dimensions and relatively short useful life due to increased wear. Therefore, Beekman proposed placing a collimator with numerous passages near the X-ray tube and having the passages' central directions originate from the same focal point in the focal spot. Based on the passages' width and length, the apparent origin of each passage will be a 'smeared out' focal point, the virtual focal spot. A sufficient number of passages is necessary to fully encompass the initial X-ray cone beam. Theoretically, when the dimensions of this collimator are chosen appropriately, the virtual focal spot perceived by the detector may be substantially smaller than the X-ray tube's actual focal spot [1].

A recent publication by Astolfo et al. roughly implemented a simplified interpretation of this concept and used an adjustable micro-scale one-dimensional slit system directly in front of the output window of a relatively large focal spot to simulate a fine focus by filtering the outer edges of the focal spot [80]. Unfortunately, the paper does not provide measurements of the consequential effective focal spot sizes acquired by this relatively simple method as confirmation, as it is not the report's primary focus. However, their attenuation, refraction, and scatter measurements at varying slit apertures suggest this simple slit method to be moderately adequate in reducing the focal spot size [80].

The method invented and patented by Beekman is a viable option for focal spot reduction of existing X-ray tubes. The idea is non-invasive on the current device, as it can be placed at the output window of the tube while also not requiring any direct electronic connection to the system. However, the exact theoretical collimator geometry has not yet been defined, and simulations have to determine the accuracy of the focal spot reduction. Therefore, this work focused on the theoretical design of the collimator as devised by Beekman. As this patent was key for this work, a shortened version is supplied in the Appendix.

2.4   Overview of Collimator Theory

A proper overview of the current collimator theory is needed to fully evaluate the possibilities of using collimation to reduce the focal spot. Collimators are used to restrict the photon acceptance angle to provide a more accurate representation of the origin of the X-ray radiation [84]. To achieve this angle restriction, holes are drilled into a piece of dense material with a relatively high attenuation coefficient. Radiation emitted in front of either of the holes and traveling in a direction approximately parallel to that hole's axis will get past the collimator. Meanwhile, the remaining radiation gets absorbed by the dense collimator material.

The holes can be filled by an interspace material, such as aluminum or carbon fiber, to attenuate the unproductive lower energetic radiation [85]. Collimators are characterized by the grid ratio - the ratio between hole length and diameter - and the grid frequency - the number of holes per cm. These together determine the total collimator sensitivity S, which is the percentage of the initial radiation transmitted through the collimator. The collimator sensitivity is important as a decreased amount of measured counts statistically decreases the SNR. To compensate for the sensitivity, either the acquisition time could be extended or, in the case of CT, the tube current could be increased [1].

For Single Photon Emission Computed Tomography (SPECT), the application of collimators is essential for the reconstruction process to determine the correspondence between a detected photon and its emission position [86]. In conventional CT, collimators are primarily used to filter out the scattered radiation, which has a known degrading effect on the image quality [87]. Since collimators are thus less essential for CT compared to SPECT, most of the current literature regarding collimators is focused on the application in SPECT. This work tries to translate the findings for SPECT collimation into helpful information for applying collimators in CT and reducing its focal spot size in particular. This subsection discusses multiple aspects of the present collimator theory.

2.4.1   Geometry

Currently, there are various collimator geometries available. The decision on which collimator to use in SPECT depends on multiple parameters, most notably the desired balance between the spatial resolution and the sensitivity [86]. In the case of scatter filtering in CT, it is the contrast resolution that benefits from collimation due to the filtering of the degrading scattered photons. For SPECT, the sensitivity is often significantly limited as only a fraction of the radiation passes through the dedicated holes, while for CT, the drop in sensitivity is generally less severe. Van Audenhaege et al. provided an in-depth review of three collimator types used for SPECT: the parallel-hole, the converging hole, and the pinhole. Even though the collimation serves a different purpose for SPECT, the several geometries could be useful for application in CT for focal spot reduction and are therefore included in this overview. Their geometry is depicted in figure 9 below [86].

Currently, most of the holes in collimators are hexagon-shaped. Other hole shapes,
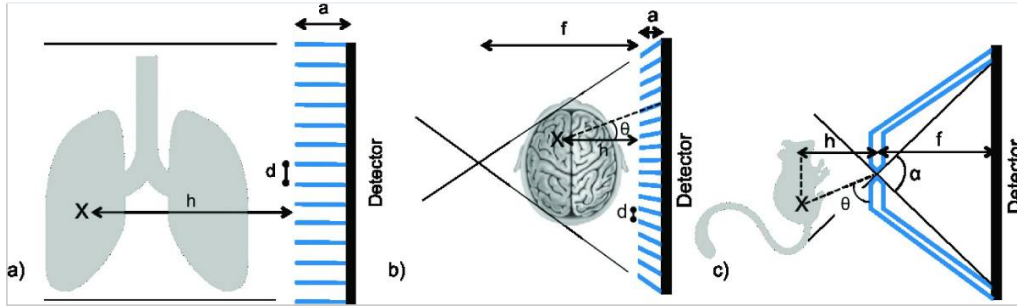
Figure 9. Transverse cut of various collimator types: a) parallel-hole collimator, b) converging hole collimator, and c) pinhole collimator [86].

such as triangles and cones, have been investigated in previous work [88, 89]. Muehllehner et al. evaluated the performance of hexagonal and triangular holes by measuring bar patterns using a simulated point source and reported negligible visual differences in image quality [88]. Beijst et al. proposed using cone-shaped holes and concluded that hexagonal holes produced a more broadened PSF than cone-shaped holes. At the same time, the cone shape also improved the contrast recovery coefficients (CRC) at equivalent noise levels [89]. However, the hexagonal shape currently remains the standard for most applications.

The parallel-hole collimator is currently still the standard in clinical practice for both SPECT and CT. Commonly, it consists of a honeycomb structure of closely packed, parallel, hexagonal-shaped holes separated by septa made of a dense material [86]. Only radiation traveling perpendicular to the entrance surface can pass through the small hexagonal regions, provided that the septal thickness does not allow for significant penetration of the radiation [86].

The converging hole collimator usually has similar hexagonal-shaped holes as the parallel-hole collimator but tilts these holes to converge their directional filtering at a specific focal point. In practice, there are two types of converging hole collimators: a fan beam collimator and a cone beam collimator. A fan beam collimator is created by only tilting the holes in the transverse plane, leaving them parallel in the axial plane, leading to a virtual focal line. A cone beam collimator consists of appropriately tilted holes in both the transverse and the axial plane, creating a virtual focal point. The radiation that gets past these collimators originates from the projection of either their focal line or focal point [86].

The pinhole collimator is often used in cases where high magnification is desired and consists of a small aperture in a plate of dense material. While common pinholes have a knife-edge profile such as the one in figure 9, the edge profile of the pinhole can vary to reduce penetration at high radiation energies [90, 91, 92]. The sensitivity of a single pinhole collimator is inherently low. However, it can be improved by introducing a collimator consisting of multiple pinholes at the cost of requiring more considerable computational power for the reconstruction process [93]. Pinhole collimators are more commonly used in preclinical research and small-animal imaging [86].

2.4.2 Materials

The choice of collimator material is driven by the need for sufficient radiation attenuation to prevent septal penetration. Septal penetration is the inevitable transmission of radiation through the septa. This phenomenon becomes a problem when the combination of the selected material's linear attenuation coefficient and the septa's thickness cannot achieve an acceptable low transmission percentage [94, 95]. For a commonly accepted septal transmission percentage limit of 5%, Sorenson and Phelps provided the following equation for the septal thickness t of a parallel-hole geometry:

$$t \gtrsim \frac{6d}{l\mu - 3} \tag{5}$$

with t the septal thickness, d the nominal hole aperture width, l the hole length, and μ the linear attenuation coefficient of the material for the specific radiation energy. Figure 10 shows an overview of these parameters and the geometry on which equation 5 is based.
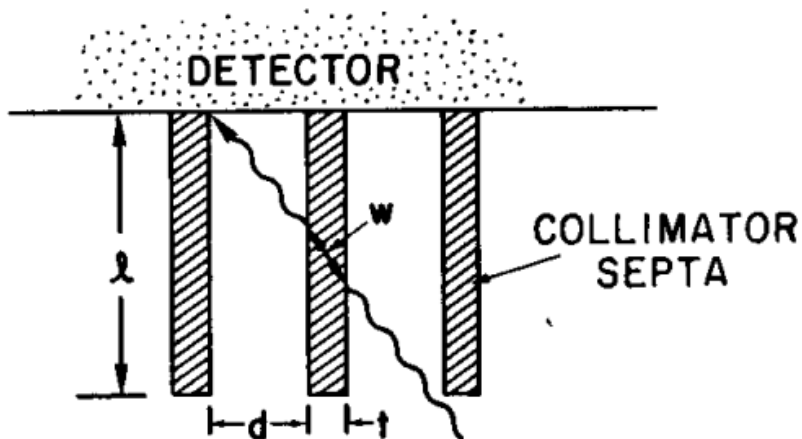
Figure 10. Schematic overview of the parameters involved with septal penetration with t the septal thickness, d the hole diameter, l the hole length, w the radiation path length through the septa and μ the linear attenuation coefficient of the material for the specific radiation energy [94].

Ideally, the septa thickness needs to be minimized to maximize the achievable sensitivity as there will be less detector area obscured [86]. Equation 5 indicates that increasing the hole length and using a material with high attenuation coefficient minimizes the needed septal thickness. Several materials have been used for this purpose, including lead, tungsten, gold, depleted uranium, and platinum [86]. In most applications, lead is the most common septal material due to its similar performance at most photon energies at a relatively low cost compared to other options [85, 96, 97]. However, Nguyen et al. studied the influence of the material choice - specifically lead, tungsten, gold, and depleted uranium - on the performance of

a pinhole collimator for a wide range of photon energies [98]. They reported that for high photon energies, lead showed an inferior resolution in combination with a lower CNR compared to the other materials, with the CNR improving up to 36.6% by using uranium. Therefore, they suggest tungsten as a sensible option for a wide range of photon energies and the use of gold inserts at higher energies [98].

2.4.3 Production

Several methods are available for the production of the described collimators. Regular parallel-hole and converging collimators are usually fabricated by stacking metal foils or casting molten metal in a mold. These techniques are both easy to execute and low in production costs, but they are limited in the minimum dimensions they can produce; about 1.2 mm hole diameter and 0.15 mm septal thickness [86]. This is sufficient for regular-resolution applications, but smaller dimensions are needed for high-resolution collimators of a smaller scale.

More precise production methods include X-ray lithography and metal electroforming, which can produce high-resolution collimators with up to 1 µm precision [86]. Makarova et al. demonstrated that the manufacturing of 25 µm thick gold septa is feasible using this technique [86, 99]. Pinhole collimators are often produced using a diamond drill system or electric discharge machining (EDM) [100]. Unfortunately, the latter techniques are costly, while complex hole shapes with required small dimensions tend to be hard to produce [86]. Recent development has shown the application of three-dimensional printing techniques using tungsten powder [101]. A selective laser melts the tungsten powder to build the desired design layer by layer, meaning complex shapes are not a limiting factor for this technique. Deprez managed to create a 96.4% pure tungsten parallel-hole collimator with a mean hole diameter of 509 µm [102]. Previously mentioned techniques would not be capable of producing a virtually pure tungsten collimator of those dimensions.

2.4.4 Current applications of collimators in CT

As previously stated, collimators fulfill a more critical role in SPECT than they do in traditional CT. Nonetheless, collimators have been a standard component of (pre-)clinical CT systems, mainly to reduce scattering effects on the image quality and avoid unnecessary dose to the subject [85, 103, 104, 105, 106, 107].

Collimators regularly used for the former purpose in CT are often referred to as anti-scatter grids and are usually relatively simple lead alloy parallel-hole collimators [108]. Anti-scatter grids are placed right in front of the detector to filter out any radiation that has been scattered along its path from tube to detector. By eliminating the scattered radiation, the contrast can be significantly increased. However, when incorrectly used, anti-scatter grids can also have deteriorating effects on the CNR, shown by both Schafer et al. and Siewerdsen et al., as it decreases the sensitivity by the inherent loss of primary photons [103, 109]. It can occasionally introduce grid line shadows to the image when using a high-resolution dynamic imaging detector depending on the grid frequency [110]. A higher dose can compensate for the

sensitivity loss but introduces another trade-off between image quality and the dose received by the subject.

Collimators are also being used to avoid unnecessary dose to the subject. For helical CT, the additional received dose due to the overlapping scanning pattern can be reduced by adaptive section collimation [111]. This is done by creating a simple hole of adjustable size in a lead slab to constrain the radiation beam onto the desired subject section, similar to the function of the X-ray tube window, which is then placed between the tube and the subject. Booij et al. reviewed a dynamically adjusting collimator incorporated into commercial Dual-Source CT systems [107]. According to their published paper, the collimation of the newest system reaches an approximately 50% efficacy of blocking the additional unnecessary dose.

Section collimation can also be used to estimate the scatter fluence in each projection directly from the pixel values near the detector edge behind the collimator leaves [104]. This approach is based on the assumption that only scattered radiation can reach the edge area of the detector that is obscured by the collimator leaves [104, 112]. The two-dimensional scatter fluence across the detector can be estimated by interpolating the edge measurements. After this, the estimated scatter fluence is subtracted from the measured projection to correct for scattering effects. Siewerdsen et al. reported a significant reduction of scattering artifacts while maintaining the CNR using this approach [104].

3 | Methods

This thesis aimed to design a convergent collimator focused on the focal spot to virtually reduce the focal spot size of an existing small-animal cone beam CT system. The detector would perceive a smaller virtual focal spot by limiting the radiation emitted outside the desired emission area from passing through a collimator. This section describes the methodology of the collimator modeling and the validation tests of its functioning.

3.1 Simulations using GATE

This work utilized the `GEANT4 Application for Tomographic Emission` (GATE) Monte-Carlo platform developed by the OpenGATE Collaboration to simulate the functioning of the designed collimator [113]. GATE was used because of its collection of powerful utilities for realistic emission tomography simulation. The relevant acquisition and simulation parameters will be supplied for the following sections.

3.2 Characteristics of the Small-Animal Computed Tomography Scanner

The simulated imaging system was based on an example small-animal computed tomography scanner, the details of which were provided at the start of this work. This subsection describes the various GATE implementations of the components of the system in more detail.

3.2.1 System geometry

The relative distances between the components of the CT scanner were vital in the design process of the collimator. The geometry of the imaging system is depicted in the schematic in figure 11 below.

The relevant system components for this work were the X-ray tube, the filter wheel, and the detector. The filter wheel, on which several filters are mounted, was rotatable around the X-ray tube. The filters can be used to filtrate low energetic radiation to reduce noisy radiation contributions to the reconstruction. Along with these filters, an opening in the wheel was present to maximize the possible magnification by enabling an object to be closer to the tube window. This opening was utilized to place the collimator as close as possible to the focal spot.
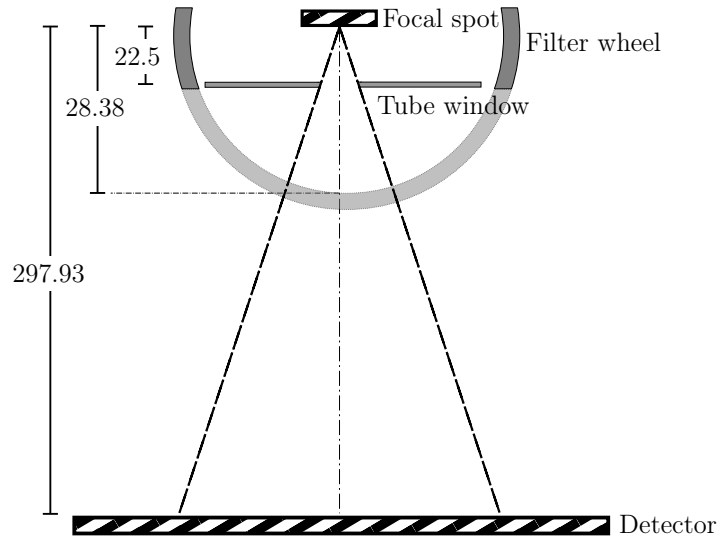
Figure 11. Schematic of the geometry of the small-animal CT scanner, showing the relative distances between the focal spot and the tube surface, lowest filter wheel edge, and the detector, respectively in mm.

3.2.2 Focal spot and cone beam

The system's focal spot was simulated as rectangularly shaped with dimensions of 30×20 µm instead of a rounded rectangle since this shape was not supported by GATE. As no actual focal spot intensity map was available, it was assumed to have a uniform intensity distribution. Figure 12 illustrates the system's focal spot map.
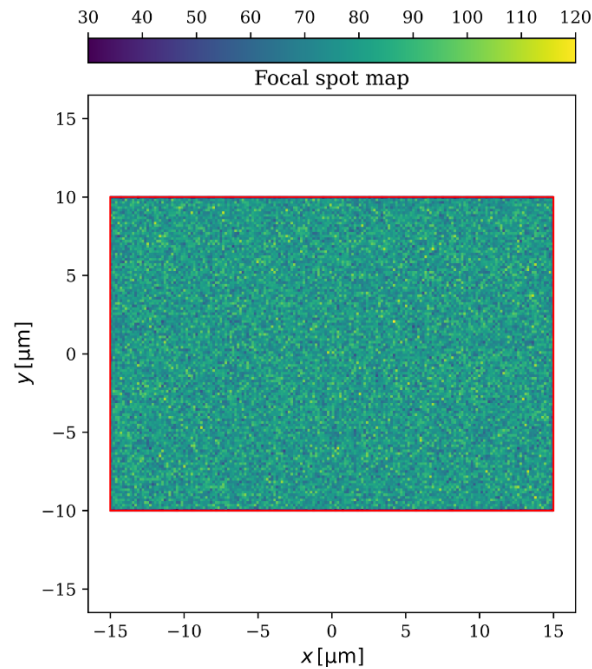
Figure 12. Exemplary focal spot intensity map of the simulated system. Simulation parameters: 10^6 emissions per s, 5 s acquisition time.

The energy spectrum of the emitted radiation was determined using the Python implementation of `SpekCalc`, which produces the energy spectrum emitted from a tungsten anode based on the tube voltage and tube current [114]. The energy spectrum resulting from using the provided system's working range of the relevant variables is shown in figure 13.
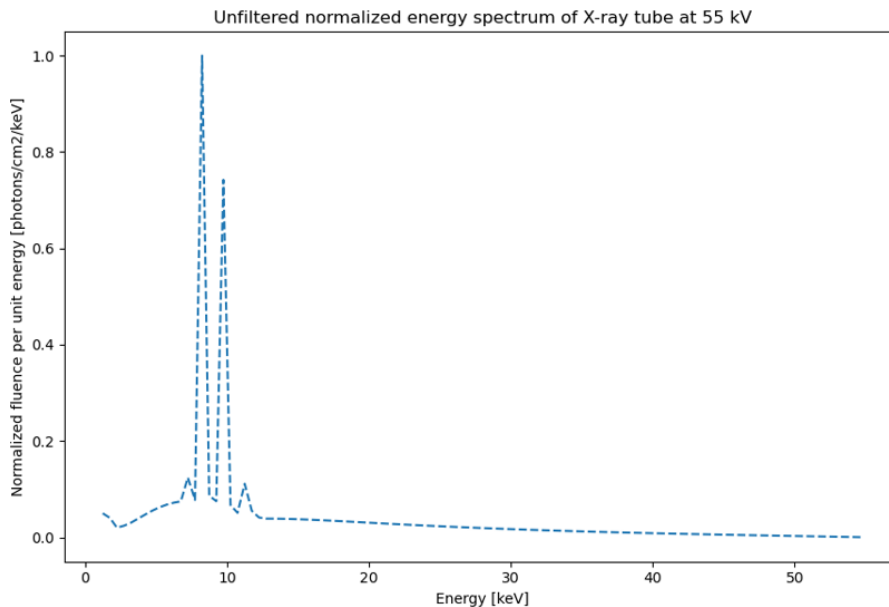
Figure 13. Emitted energy spectrum of the focal spot during simulations, calculated by `SpekCalc`. Simulation parameters: 55 kV tube potential, 0.22 mA tube current, 25 deg anode angle θ.

The focal spot emitted a cone beam through a beryllium window of 0.5 mm thickness, followed by a 0.1 mm aluminum protection filter as the outer layer of the tube window. In a realistic simulation, the cone angle of the beam C_α should be large enough to fully irradiate the whole detector plane, which would be 13.7 deg for this system. Unfortunately, due to computational memory limitations induced by GATE, the cone angle had to be limited to 0.25 deg, which was insufficient for total irradiation and resulted in a small field-of-view (FOV). Nonetheless, the small FOV was still used to evaluate the functioning of the collimator to reduce the penumbra. Figure 14 illustrates a schematic of the simulated cone beam, where *FTD* is the focus-tube-distance, and *TDD* is the tube-detector distance. The penumbra effect can be seen to alter the edge response of the projection due to the finite size of the focal spot.

3.2.3 Detector

The system has a cesium iodide (CsI) scintillation detector for radiation detection, which dimensions are 145.4 × 114.9 × 0.15 mm. The detector has a pixel size of 74.8 × 74.4 µm.
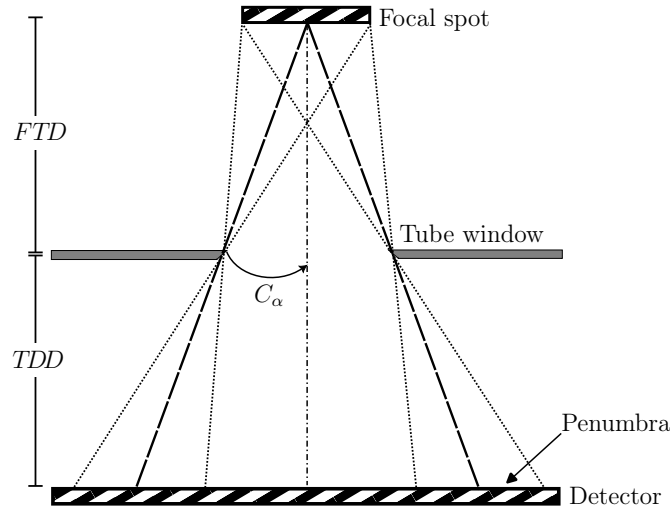
Figure 14. Schematic of the cone beam, where cone angle C_α is 0.25 deg. Due to the finite size of the focal spot, the penumbra effect influences the edge response of the projection.

3.3 Design of the Collimator for Reduction of the Focal Spot Size

The following subsection describes the design process of the desired collimator. It includes the theoretical derivation of the relevant dimensions and simplified explanations of the computational algorithms used.

3.3.1 Initial requirements

Several initial requirements needed to be taken into account during the design process. These requirements have already been mentioned before, but they are summarized below for clarity.

- The collimator must be introduced to an existing CT system without integral changes to the X-ray tube.

- The collimator needs to be a viable alternative to fully replacing the X-ray tube for a tube with a smaller focal spot.

- The virtual focal spot needs to be a similar or more favorable focal spot intensity map than a regular focal spot of equal nominal size.

These requirements were leading during decisions regarding the optimization of the collimator and will be referred to in the following subsections.

3.3.2 General concept

The approach of this thesis was to design a convergent collimator focused on the focal spot to virtually reduce the focal spot's size, depicted in figure 15 below.
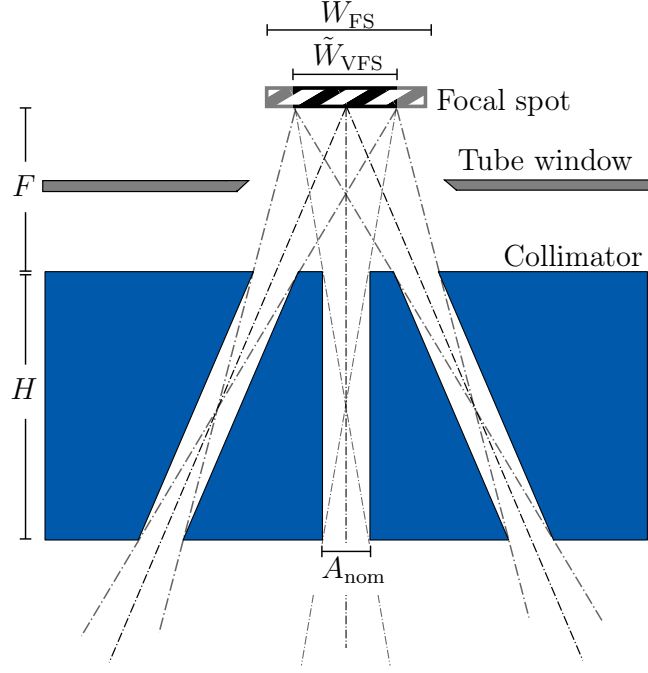
Figure 15. Concept of a simplified converging collimator virtually reducing the focal spot width W_FS. The virtual focal spot width $\tilde{W}_\mathrm{VFS}$ is dependent on the focal distance F, the collimator height H, and the nominal hole aperture width A_nom. Only emissions originating from $\tilde{W}_\mathrm{VFS}$ are permitted through the collimator.

By focusing numerous sufficiently small holes at the center of the focal spot, only the projections emitted by an arbitrarily smaller area of the focal spot are allowed to reach the detector. The septa would attenuate emissions originating from outside this virtual focal spot. The number of holes was maximized to maximize the total collimator sensitivity S.

3.3.3 Virtual focal spot width

The effective focal spot will now be referred to as the focal spot for clarity. The virtual focal spot width $\tilde{W}_\mathrm{VFS}$ was set to be the nominal width of the desired reduced focal spot. Based on the similar triangles in figure 15, $\tilde{W}_\mathrm{VFS}$ was determined to be related to the focal length F, the collimator height H and the nominal hole aperture width A_nom, which is the maximum width in the relevant cross-section, as follows:

$$\tilde{W}_\mathrm{VFS} = A_\mathrm{nom} \left(\frac{2F}{H} + 1 \right) \tag{6}$$

To satisfy the second design requirement and make the production of the collimator feasible, maximizing A_nom was beneficial to reduce production complexity as larger holes would be easier to produce. In that case, it is evident from equation 6 that the focal length F needs to be minimized while maximizing the hole height H for a specific desired virtual focal spot width $\tilde{W}_\mathrm{VFS}$.

3.3.4   Septal thickness and material

Lead was used as the septum material due to its high linear attenuation coefficient and low cost relative to alternatives with similar attenuation performance. To determine the needed septal thickness, the maximum permitted septal penetration $T_{\max}$ was defined as:

$$T_{\max} = e^{-\mu P_{\min}} \tag{7}$$

where μ is the linear attenuation coefficient of lead and $P_{\min}$ is the corresponding minimum path length through the lead septa that needs to be traversed by the radiation. This work adhered to the value of 5% for $T_{\max}$, which is the standard across the literature. The minimal possible path through the septa is visualized in figure 16, and depends on the septal thickness t and hole angle α.
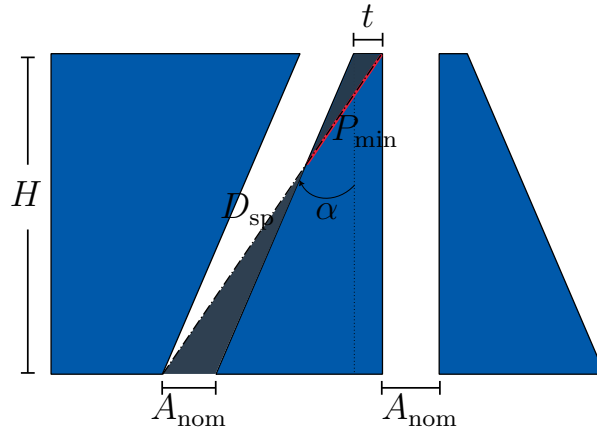
Figure 16. Schematic of the septal penetration based on the septal thickness t, the hole angle α, hole height H, the minimum path length $P_{\min}$, and the nominal hole aperture width along the cross-section A_{nom}. The shaded areas are similar triangles, and $P_{\min}$ is highlighted in red.

The shaded similar triangles were used to determine the minimum t needed to obtain the desired $T_{\max}$ by first expressing the dotted diagonal D_{sp} in terms of t, α, A_{nom}, and H:

$$D_{\mathrm{sp}} = \sqrt{H^2 + (H \tan \alpha + t + A_{\mathrm{nom}})^2} \tag{8}$$

and by then using this to phrase the similar triangles equation as:

$$\frac{t}{A_{\mathrm{nom}}} = \frac{P_{\min}}{D_{\mathrm{sp}} - P_{\min}} \tag{9}$$

Finally, rewriting and substituting equation 7 and 8 into equation 10 produces the equation to solve for t:

$$\frac{t}{A_{\text{nom}}} = \frac{-\ln T_{\text{max}}}{\mu\sqrt{H^2 + (H\tan\alpha + t + A_{\text{nom}})^2} + \ln T_{\text{max}}} \tag{10}$$

Equation 10 was solved by using the algebraic computation package `SciPy` for Python for each specific hole.

3.3.5 Dimensions and Geometry of Collimator

This work followed the currently standard collimator design by using hexagon-shaped holes of air in a honeycomb pattern, which maximizes the hole density of the collimator, as illustrated in figure 17.
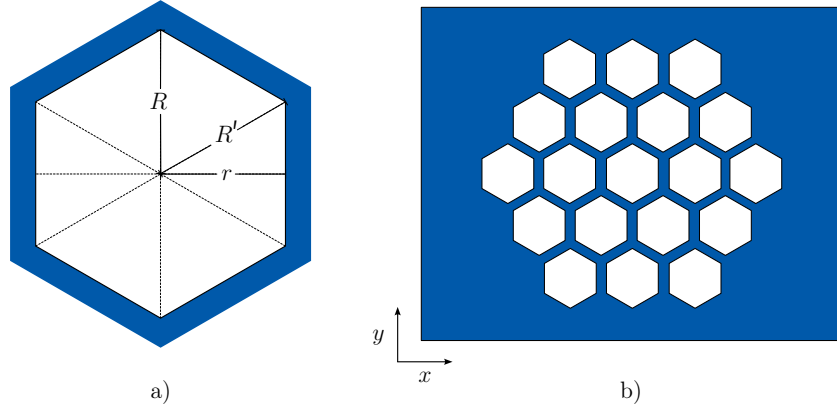
Figure 17. Simplified representations of the collimator holes: a) the base hole aperture with R being the vertical outer radius, r the inner radius, and R' the diagonal outer radius; b) circular honeycomb hole placement grid as seen from the top of the collimator

The relation between R and r is given by $r = \frac{\sqrt{3}}{2}R$, indicating that the nominal hole aperture width in the x-direction $A_{\text{nom,x}}$ is smaller than in the y-direction $A_{\text{nom,y}}$, which will be utilized in the algorithm's explanation later on. The desired virtual focal spot width $\tilde{W}_{\text{VFS}}$ was chosen to be 10 µm. To maximize A_{nom}, as discussed before, to satisfy the design criterion of production feasibility while also adhering to the requirement of no integral changes to the X-ray tube, the collimator needed to be as close to the tube surface as possible, thus, minimizing F. It was determined that the opening in the filter wheel was the most logical option for placing the collimator. Therefore, F was set at 22.6 mm and H to 5.5 mm to fit precisely into the filter wheel opening, which will be illustrated later.

All the holes were tilted by hole angle α to focus their central axis on the center of the focal spot. These angles were determined by F and the center position of the hole apertures at the top level of the collimator by the following equation:

$$\alpha = \tan^{-1}\left(\frac{\sqrt{x^2 + y^2}}{F}\right) \text{ with } \alpha_x = \tan^{-1}\left(\frac{x}{F}\right) \text{ and } \alpha_y = \tan^{-1}\left(\frac{y}{F}\right) \tag{11}$$

where x and y are the distances of the top hole apertures' centers relative to the center of the current focal spot, $\alpha_{x,y}$ the projection of the hole angle along the respective axis, and the focal distance F the distance from the current focal spot to the collimator. As illustrated in figure 15, the tilted holes were elongated to reach the full height of the collimator, after which the protruded sections were cut off.

Using equation 6 and the set values, A_{nom} could be calculated. The nominal width A_{nom} of a hexagon, the maximum width along any cross-section, is usually equal to twice the outer radius R; however, due to the hole's tilt, the shape of the aperture was outstretched perpendicular to its rotation axis. Therefore, A_{nom} was dependent on α and its rotation axis. The A_{nom} of the stretched aperture was determined equal to:

$$A_{\text{nom}} = 2R \max \left\{ \frac{1}{\cos \alpha_y}, \sqrt{\frac{3}{4 \cos^2 \alpha_x} + \frac{1}{4 \cos^2 \alpha_y}} \right\} \qquad (12)$$

where the first max-term is based on the stretch of the vertical R, and the second term is on the stretch of the diagonal R'. As A_{nom} stretches due to the hole's tilt, the virtual focal spot width $\tilde{W}_{\text{VFS}}$ projected through the respective hole increases as well. To ensure a constant $\tilde{W}_{\text{VFS}}$ through all individual holes, the hole outer radii R were dynamically adjusted by the inverse of the max-function in equation 12 to equalize A_{nom} of all the holes to its constant base value given by equation 6.

3.4   Collimator Generation by Python Algorithm

A Python algorithm was developed to generate the collimator geometry automatically after supplying the necessary input variables. Their set values are summarized in table 3.1 below.

Table 3.1. Summary of the set values used as input to the developed Python algorithm.

Parameter	Value
Virtual focal spot width $\tilde{W}_{\text{VFS}}$	10 µm
Hole height H	5.5 mm
Focal length F	22.6 mm
Cone angle C_α	0.25 deg
Maximum septal penetration T_{max}	5%

Figure 18 shows the generic approach to determine the hole position grid. By first calculating the position of the holes along the x-axis and then using the holes along the y-axis to find the y-position of each row, the grid was found by meshing the found x- and y-coordinates into a honeycomb pattern. The following subsections will elaborate on these calculations.
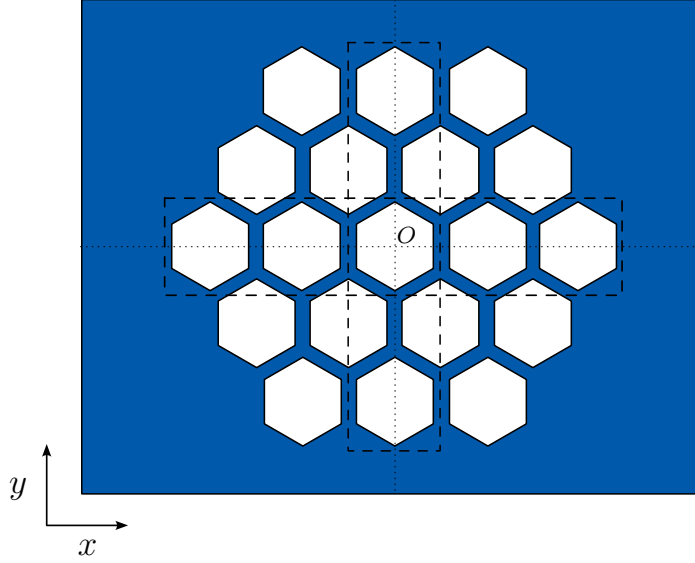
Figure 18. Schematic of the algorithm's approach to creating the hole position grid. The center hole row along the x-axis was determined, after which the y-position of the other rows was calculated. By meshing these, the honeycomb hole position grid was formed.

3.4.1 Determining X-positions of grid

Figure 19 illustrates the iterative algorithm to determine the x-positions of the grid.
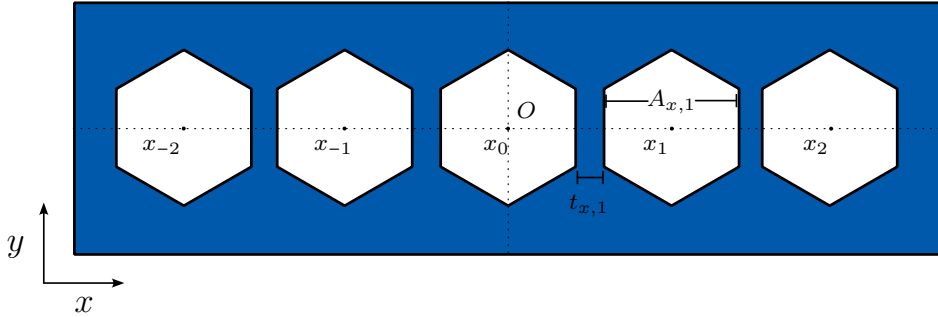
Figure 19. Visualization of the center row at $y = 0$ in the x-direction on which the determination of the x-coordinates is based. $A_{x,i}$ is the aperture width in the x-direction of hole i, and $t_{x,i}$ the septal thickness in the x-direction of the i-th hole.

The algorithm started by calculating the hole x-positions of the collimator's center row at $(y = 0)$ in the $(z = F)$-plane. It was starting from the center hole (x_0) at $(x = 0, y = 0)$ with the focal spot correspondingly centered at $(x = 0, y = 0)$ in the $(z = 0)$-plane. The most outer x-position $x_{\max}$ was established by the cone angle C_α and focal length F, as the most outer hole angle $\alpha_{\max}$ did not need to exceed C_α. The algorithm iteratively determined the x-position of the next adjacent hole until the stop criterion of $x_i > x_{\max}$ was reached. For each adjacent hole i until $i_{\max}$, `SciPy` was used to solve the following set of equations to find x_i:

$$
\begin{cases}
\alpha_{x,i} = \tan^{-1}\left(\dfrac{x_i}{F}\right) \\[4mm]
A_{\mathrm{x},i} = \dfrac{\sqrt{3}}{2}\dfrac{\tilde{W}_{\mathrm{VFS}}}{\left(\frac{2F}{H}+1\right)}\dfrac{1}{\sqrt{\frac{3}{4\cos^2\alpha_{x,i}}+\frac{1}{4}}}\dfrac{1}{\cos\alpha_{x,i}} \\[4mm]
t_{x,i} = x_i - \left(x_{i-1} + \dfrac{A_{\mathrm{x},i-1}}{2}\right) - \dfrac{A_{\mathrm{x},i}}{2} \\[4mm]
\dfrac{t_{x,i}}{A_{\mathrm{x},i}} = \dfrac{-\ln T_{\max}}{\mu\sqrt{H^2 + (H\tan\alpha_{x,i} + t_{x,i} + A_{\mathrm{x},i})^2} + \ln T_{\max}}
\end{cases}
\tag{13}
$$

which are a combination of the equations derived in the previous section. After stopping at $i_{\max}$, the found x_i were then mirrored to x_{-i} around the center hole to establish the full center row hole x-coordinates. The grid's honeycomb pattern was created by alternating rows compassing these found x-coordinates with rows using their intermediary x-coordinates.

3.4.2 Determining Y-positions of grid

Figure 20 illustrates the iterative algorithm to determine the y-positions of the grid.
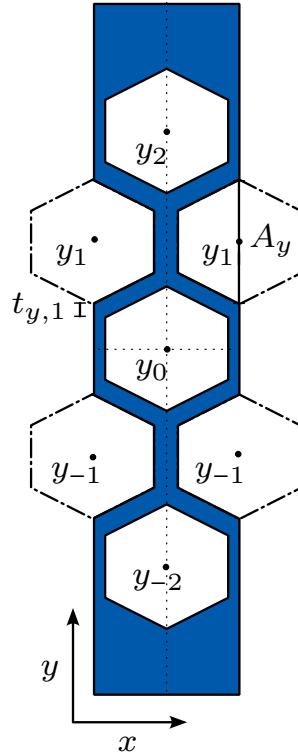
Figure 20. Visualization of the center row in the y-direction on which the determination of the y-coordinates is based. A_y is the aperture width in the y-direction, and t_y the septal thickness in the y-direction.

The y-component of the septal thickness $t_{y,j}$ needed to be equal to $\frac{\sqrt{3}}{2} t_{x,i}$ to ensure uniform septal thickness surrounding the holes. In addition, as the outer radius R of the holes lined up with the y-axis, the cosine factors of equation 12 and the dynamically adjusted outer radius canceled each other. These insights made the y-coordinates more trivial to calculate by looking at the center row in the y-direction. From figure 20, it can be deduced that the y-position of the rows y_j, starting from the center row ($y = 0$, $j = 0$) and again until $y_j > y_{\max}$, could be calculated as:

$$
\begin{cases}
A_y = \dfrac{\tilde{W}_{\mathrm{VFS}}}{\left(\frac{2F}{H} + 1\right)} \\[2ex]
t_{y,j} = \dfrac{\sqrt{3}}{2} t_{x,i} \\[2ex]
y_j = y_{j-1} + t_{y,j} + \dfrac{3}{4} A_y
\end{cases}
\tag{14}
$$

3.4.3 GATE implementation of collimator

The collimator was implemented in GATE by creating a rectangular lead base of $12 \times 12 \times 5.5$ mm, in which all the air holes were individually placed. The final geometry of the simulated system is depicted in figure 21 below.
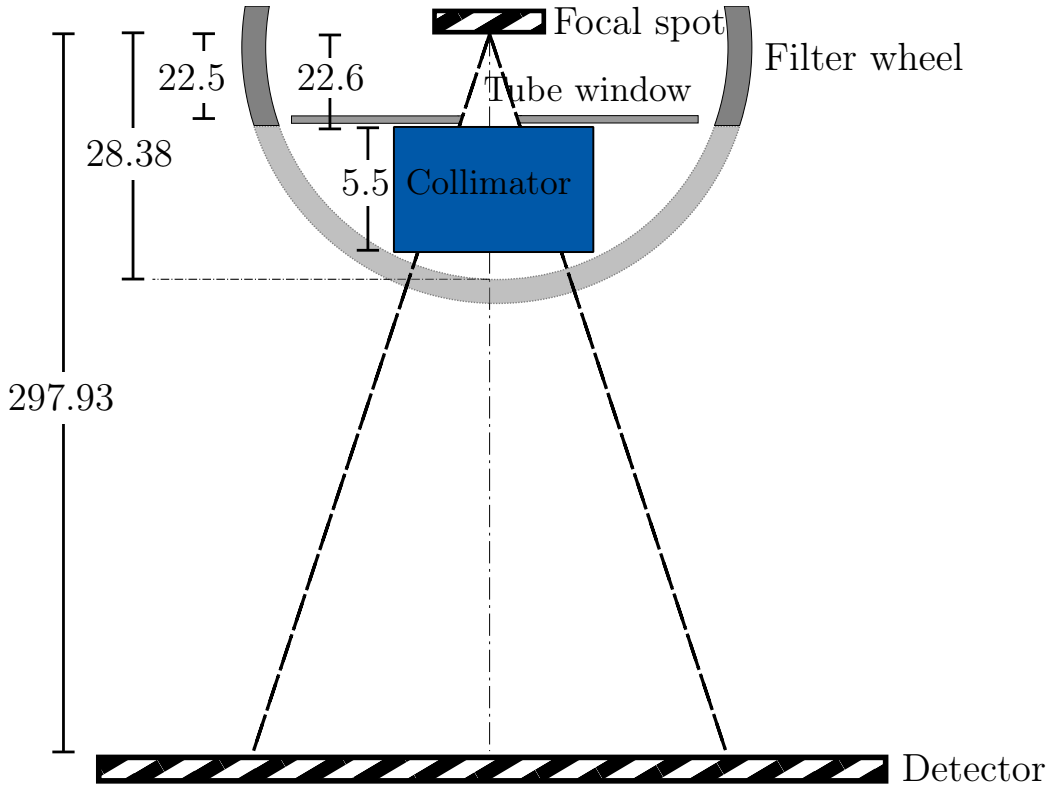
Figure 21. Schematic of the simulated system geometry, including the collimator. The collimator is placed close to the tube window while fitting precisely within the filter wheel radius. All distances are in mm.

3.5 Validation of Collimator Efficacy

Several validation tests were conducted to verify the theoretical collimation principle and compare the virtual focal spot's performance to its reference counterpart without the collimator. Various simulations that included the designed collimator were run for different acquisition times. The following subsection will discuss these tests in more detail.

3.5.1 Reference data

The reference data were simulated by omitting the collimator and running a 5-second acquisition without any phantom using the standard system. Using histograms, the simulation acquired a reference projection measurement and several intermediate virtual projections. These were obtained by virtual detectors between the focal spot and the actual detector - without altering the radiation beam - and were used to calculate relevant physical quantities, such as introduced scatter.

3.5.2 Proof of concept: virtual focal spot map

The virtual focal spot map resulting from a 5-second acquisition was analyzed based on theoretical expectations on its distribution, shown in figure 22.
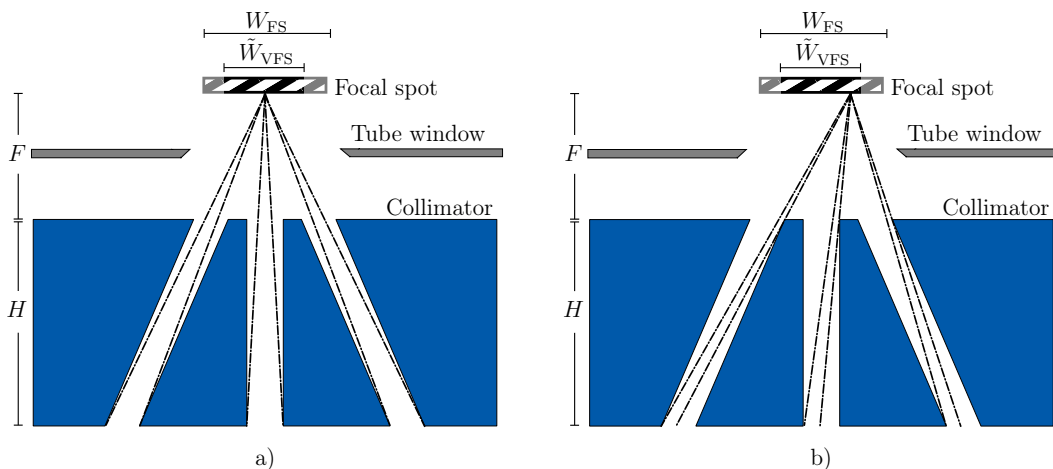
Figure 22. Illustration of the theoretical expected focal spot distribution. The center emissions in a) fully irradiate the holes, while off-center emissions shown in b) fail to completely irradiate the aperture.

A Gaussian-like focal spot distribution was anticipated due to the collimator's geometry only transmitting a fragment of the radiation when emitted near the edge of the desired virtual focal spot compared to its center, shown by the diagrams in figure 22. The off-center emissions fail to irradiate the holes fully, showing a decrease in collimator sensitivity S related to the emission's distance to the focal spot center. Thus, the focal spot intensity map keeps diminishing towards the edge of the desired virtual focal spot, which resembles a Gaussian distribution. Therefore, a 2D Gaussian distribution with amplitude I_G was fitted to the measured histogram focal spot map by `SciPy`, where I_G was taken as the measure for the transmitted

count intensity of the virtual focal spot's center and $\sigma_{x,y}$ as the standard deviations of the Gaussian distribution in x- and y-direction. The goodness of fit was measured by the well-established coefficient of determination CD^2:

$$CD^2 = 1 - \frac{\sum_i (h_i - G_i)^2}{\sum_i (h_i - \bar{h})^2} \tag{15}$$

where h_i are the measured histogram values of the focal spot, G_i the corresponding predicted values by the Gaussian fit, and $\bar{h}$ the mean over the histogram measurements.

The shape and size of the virtual focal spot were assessed visually in addition to the quantitative full-width-at-half-maximum (FWHM) and the percentage of counts inside the wanted hexagonal area. For Gaussian distributions, the standard deviation and FWHM are related as:

$$FWHM = 2\sqrt{2\ln 2}\,\sigma \tag{16}$$

Therefore, the FWHM of the virtual focal spot in both x- and y-direction were determined by their standard deviation σ_x and σ_y, respectively.

The practical collimator center sensitivity $\tilde{S}_c$ could be deduced by dividing I_G by the average intensity of the reference focal spot I_{ref}. The theoretical collimator center sensitivity of the focal spot's center S_c can be derived from the diagram on the left, as the ratio between the total area of the bottom hexagon-shaped apertures and the cross-sectional area of the non-collimated cone beam at the bottom of the collimator, and was shown equal to:

$$S_c = \frac{3\sqrt{3}\,A_{\mathrm{nom}}{}^2\,N_h}{2\pi\,(F + H)^2 \tan^2 C_\alpha} \tag{17}$$

where N_h is the total amount of holes in the collimator, F the focal length, H the collimator height, C_α the cone angle, and A_{nom} the nominal aperture width. The theoretical and practical sensitivities were compared for proof of concept by dividing them and checking whether it does not exceed the maximum permitted septal penetration T_{max} threshold:

$$\frac{\tilde{S}_c}{S_c} \leq 1 + T_{\mathrm{max}} \tag{18}$$

3.5.3   Evaluation of single projection

The projections resulting from the virtual focal spot with various acquisition times were evaluated and compared to the reference projection. The SNR was obtained for each projection by taking the mean and standard deviation of a specified area

inside the circular projection and then dividing them. In addition to the SNR, each projection's total number of counts N_{counts} was also documented. N_{counts} was used to calculate the total collimator sensitivity S, which was given by the ratio between the collimated projection's number of counts $N_{\text{counts,VFS}}$ and the number of counts of the reference without collimator $N_{\text{counts,ref}}$. Based on the discovered collimator sensitivity S, a count-equivalent projection by the virtual focal spot was acquired by scaling the acquisition time with S. This count-equivalent projection was then compared to the reference in terms of SNR and visual appearance.

Theoretical projection radius
Figure 23 illustrates the reference projection resulting from the cone beam with C_α.
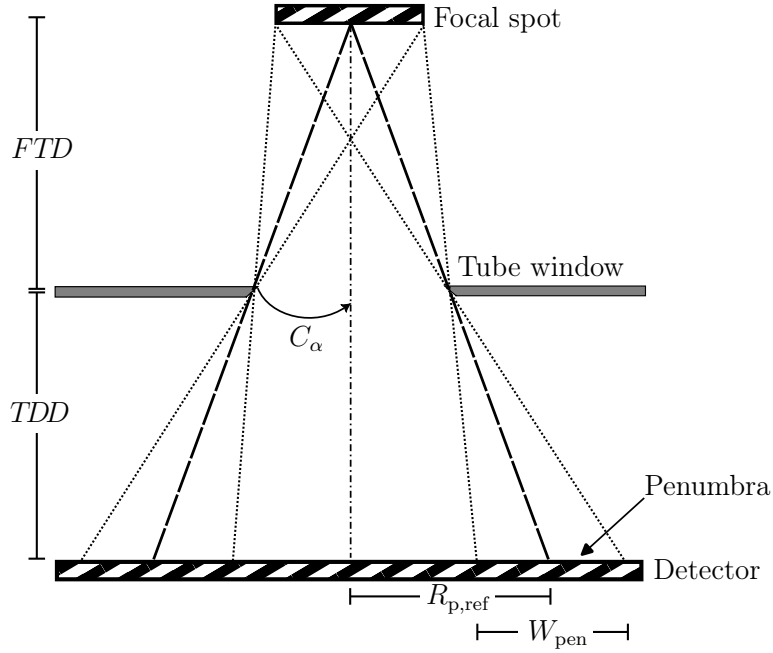
Figure 23. Schematic of the reference cone beam projection, where cone angle C_α is 0.25 deg. The theoretical radius of the reference projection $R_{\text{p,ref}}$ and the penumbra width W_{pen} were calculated and used as visual indicators.

The theoretical radius of the reference projection $R_{\text{p,ref}}$ was determined by:

$$R_{\text{p,ref}} = (FTD + TDD) \tan C_\alpha \tag{19}$$

with FTD the focus-tube distance, and TDD the tube-detector distance and C_α the cone angle. The theoretical penumbra width W_{pen} was calculated using:

$$W_{\text{pen}} = W_{\text{FS}} \frac{TDD}{FTD} \tag{20}$$

$R_{\text{p,ref}}$, along with an overlaid penumbra width W_{pen}, was used as a visual indicator during the validation of reference projections. For collimated projections, $\tilde{W}_{\text{VFS}}$ and $\alpha_{\max}$ substituted their corresponding counterparts.

3.5.4 Reduction of penumbra effect

This work aimed to find an alternative to reduce the focal spot size, thus, reducing the penumbra effect on the resulting projections. An enlarged view of the projection's edges was obtained to visualize the penumbra effect. An example of this enlarged view is pictured in figure 24.
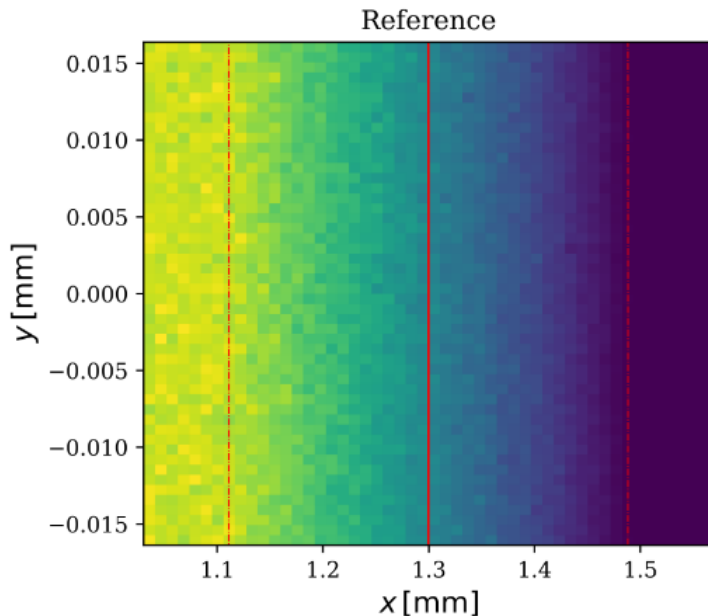
Figure 24. Enlarged view of the projection edge on the x-axis. The red line indicates the theoretical projection radius $R_{\mathrm{p,ref}}$, and the dotted lines represent the theoretical penumbra limits.

The edge response was acquired by adding the measurement values in the appropriate direction into a 1D array for the virtual focal spot and the reference projection, then normalizing them around the theoretical projection radius $R_{\mathrm{p,ref}}$ found from equation 19. They were then plotted in the same figure, along with the theoretical edge response, for visual comparison. The theoretical edge response was based on the expectation of a linear edge response function between a uniform focal spot's penumbra width W_{pen}. W_{pen} was calculated using the equation 20 and a normalized linear function was drawn between the edges of the W_{pen} to illustrate the theoretical edge response for both the reference focal spot and the virtual focal spot.

3.5.5 Scattered radiation after collimator

The scatter radiation leaving the collimator was approximated by obtaining the scatter at the exit of the collimator volume when the collimator is or is not present. This exit scatter was determined by checking for each particle entering the volume whether its direction vector at emission was different when passing the exit plane of the collimator. The element-wise difference between the x-, y- and z-components of the emission direction vectors and the exiting direction vectors were checked to be under a specified permitted error ϵ. When that was the case for all three the

36

coordinate-components, the exiting photon was labeled as primary radiation. The final measure was to obtain the percentage of the exiting photons being attributed as primary radiation. The determination of an appropriate value for ϵ was done by repeating the process for multiple values of ϵ, ranging from 2 to $2 \cdot 10^{-13}$ in logarithmic spacing, and selecting the value for which the percentage is assumed to stay constant before being subject to float-precision error.

4 | Results

4.1 Evaluation of Projection and Focal Spot Map

This subsection evaluates the different simulations. The histograms for the projection and focal spot maps utilized 125×125 and 200×200 bins, respectively.

4.1.1 Reference measurement (5 Seconds)

The reference measurement's projection and focal spot map are displayed in figure 25.
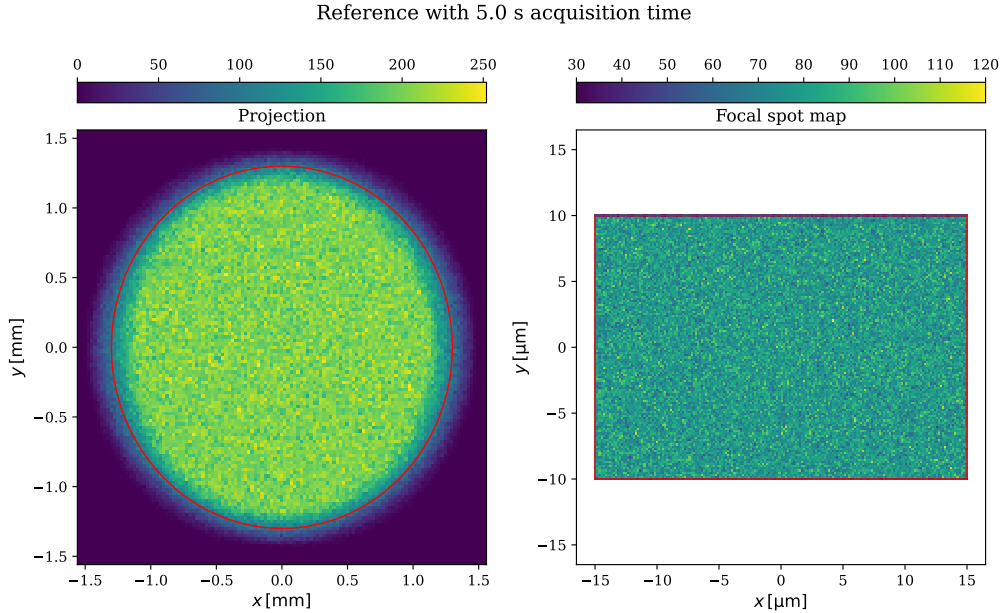
Figure 25. Reference measurement's projection and focal spot intensity map after a 5-second acquisition. The red lines indicate the theoretical projection radius $R_{\mathrm{p,ref}}$ on the left and the initial simulated focal spot shape on the right. Projection: SNR of 13.86 and total counts $N_{\mathrm{counts,ref}}$ of 1733826 counts. Focal spot: mean intensity I_{ref} of 78.81 counts.

The projection visibly showed the penumbra effect, due to the finite size of the focal spot, at the edges around the theoretical projection radius $R_{\mathrm{p,ref}}$, shown as the red line. The projection had a SNR of 13.86, with a total of 1733826 counts measured. The reference focal spot map showed the initialized size of 30×20 µm, and a mean intensity I_{ref} of 78.81 counts was measured over the uniformly distributed map.

4.1.2 Virtual focal spot measurement (5 Seconds)

Figure 26 illustrates the virtual focal spot measurement results by employing the designed collimator.
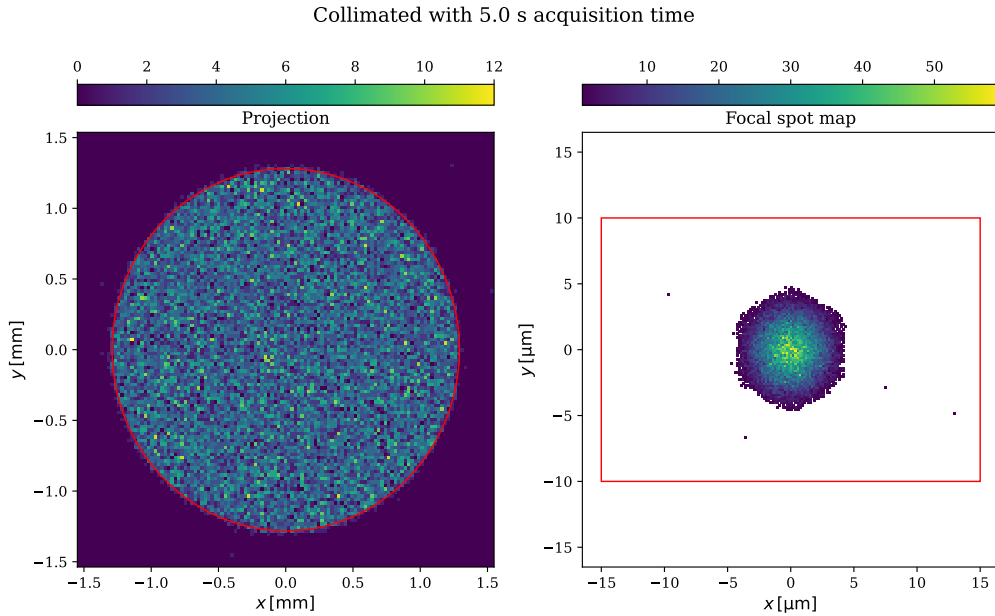
Figure 26. Virtual focal spot measurement's projection and focal spot intensity map after a 5-second acquisition. The red lines indicate the theoretical projection radius $R_{\text{p,ref}}$ on the left, and the initial simulated focal spot shape on the right. The fitted 2D Gaussian distribution had a coefficient of determination CD^2 of 0.95, showing high goodness of fit. Projection: SNR of 1.91 and total counts $N_{\text{counts,VFS}}$ of 32116 counts. Focal spot: fitted center intensity I_{G} of 44.88 counts and FWHM of [4.24, 4.29] µm.

When visually assessed, it is evident that the collimator successfully reduced the focal spot size, reinforced by the fact that 99.09% of the measured counts originated from the desired area. The virtual focal spot width $\tilde{W}_{\text{VFS}}$ can be seen to correspond to the intended 10 µm, and the focal spot's distribution did closely resemble the anticipated 2D Gaussian, shown by the coefficient of determination's high value. The FWHM in x- and y-direction were 4.29 and 4.24 µm, respectively, which were under the foreseen value of 5 µm. This was most likely due to the light tail of the fitted 2D Gaussian distribution, as the hexagon-shaped focal spot comprises hard cut-off edges of the smooth Gaussian, in addition to the smaller aperture width in the x-dimension due to its smaller inner radius r. This possibly slightly altered the distribution towards a light tail and, thus, induced a smaller standard deviation.

The collimator's measured practical center sensitivity $\tilde{S}_c$ was equal to 56.94%, which complied with equation 18, as the theoretical center sensitivity was estimated to be 55.44%. This result indicated that even thinner septa would theoretically suffice to meet the set maximum permitted septal penetration T_{max} of 5%. As mentioned

in the Methods, the total collimator sensitivity S was determined by dividing the number of counts in the virtual focal spot projection $N_{\mathrm{count,VFS}}$ by the number of counts in the reference $N_{\mathrm{count,ref}}$. This led to an S of only 1.85%, which shows in the low signal, noisy projection produced, with a SNR of only 1.91. To obtain a comparable amount of counts using the collimator, the acquisition needs to be up-scaled by a factor of ~ 54. The Theory section described that this could be done by increasing the tube current or the acquisition time. Therefore, the measurement was reprised for 270 seconds to obtain a reference-equivalent virtual focal spot projection for comparison.

4.1.3 Virtual focal spot measurement (270 seconds)

The final virtual focal spot measurement's projection and focal spot map are presented below in figure 27.
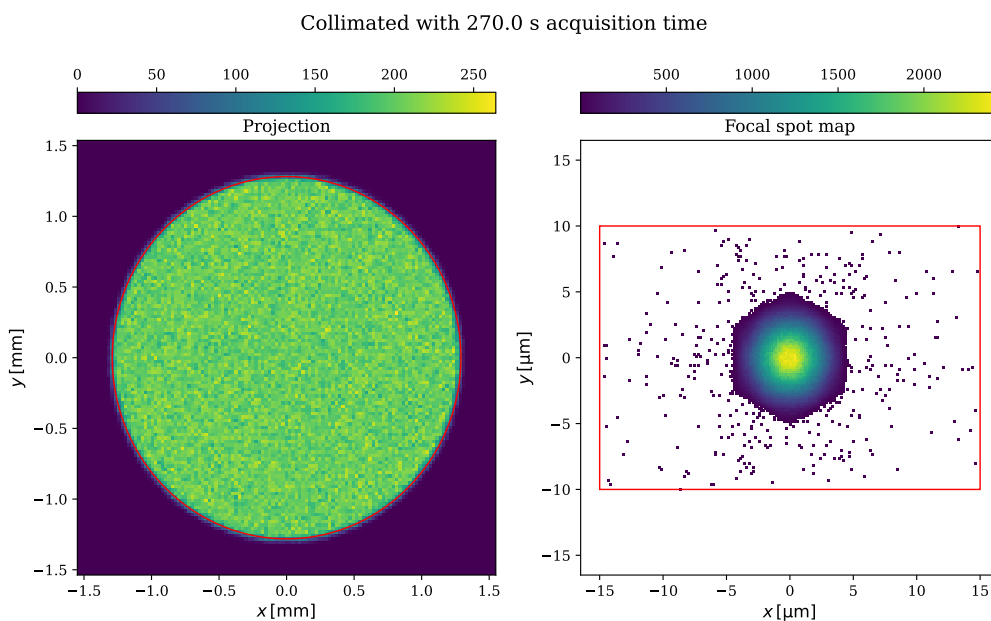
Figure 27. Virtual focal spot measurement's projection and focal spot intensity map after a 270-second acquisition. The red lines indicate the theoretical projection radius $R_{\mathrm{p,ref}}$ on the left, and the initial simulated focal spot shape on the right. The fitted 2D Gaussian distribution had a coefficient of determination CD^2 of 0.99, showing very high goodness of fit. Projection: SNR of 14.27 and total counts $N_{\mathrm{counts,VFS}}$ of 1735512 counts. Focal spot: fitted center intensity I_{G} of 2441 counts and FWHM of [4.24, 4.25] µm.

The 270-second projection succeeded in having an almost equal number of counts compared to the reference projection, and the SNR was slightly improved to 14.29. A visual inspection of figure 27 and the reference quickly leads to the conclusion that the penumbra effect was significantly reduced and is barely visibly present in the virtual focal spot projection, proving the concept of the collimator.

The focal spot's expected Gaussian distribution was clearly visible, and 99.2% of the counts were inside the wanted hexagonal area. The FWHM in both directions was almost identical to the 5-second measurement, reconfirming the assumption that its lower-than-anticipated value is indeed not count-related but rather a matter of hole geometry.

4.2 Reduction of penumbra effect

An overview of the enlarged views of the projection edges was supplied in figure 28, for the x-direction and the y-direction.
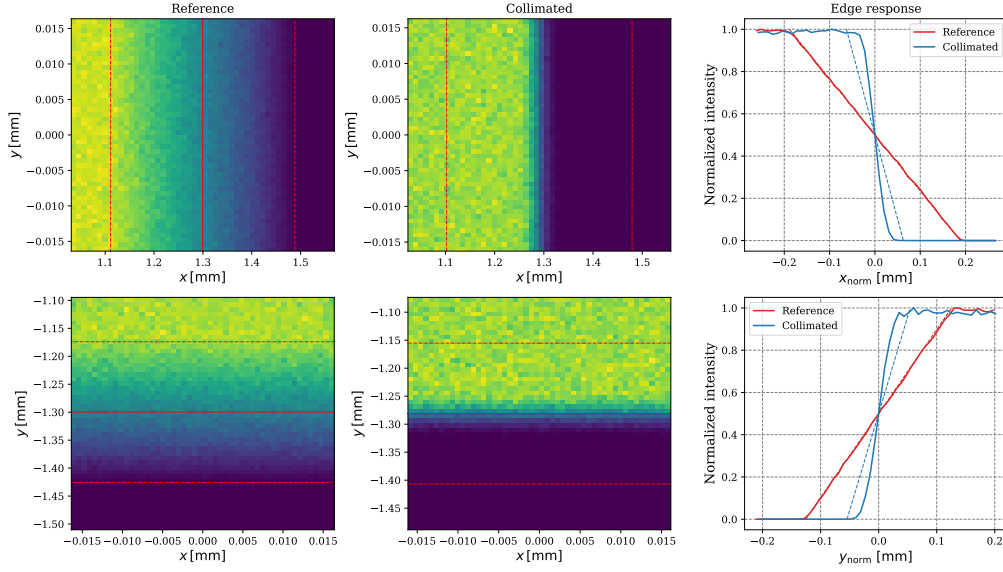
Figure 28. Overview of the enlarged views of the projection edges to analyze the penumbra effect in more detail. In the first two columns, the red line indicates the theoretical projection radius of the reference $R_{\mathrm{p,ref}}$, and the dotted lines represent the theoretical penumbra limits. The last column illustrates the edge response curve of the reference and the collimated projection with the solid lines. The dotted lines indicate their theoretical linear edge response.

The enlarged views emphasized the reduction of the penumbra effect by the designed collimator. The collimator's edge response outperformed the theoretical edge response from an actual focal spot with a nominal width of 10 µm, as seen by its more abrupt edge response. This was most likely due to its Gaussian distributed intensity map, highlighting the center of the virtual focal spot, compared to the linear edge response function from a uniform distributed intensity map.

Due to the nominal aperture width in the x-direction A_x being $\frac{\sqrt{3}}{2}$ times smaller than the nominal aperture width in the y-direction A_y, the effective penumbra reduction was more prominent in the x-direction. This suggests that the collimator's x-axis should be aligned with the largest dimension of the actual focal spot to maximize the attainable virtual size reduction.

41

4.3 Scattered radiation after collimator

The results of the described scatter measurements are depicted below in figure 29.
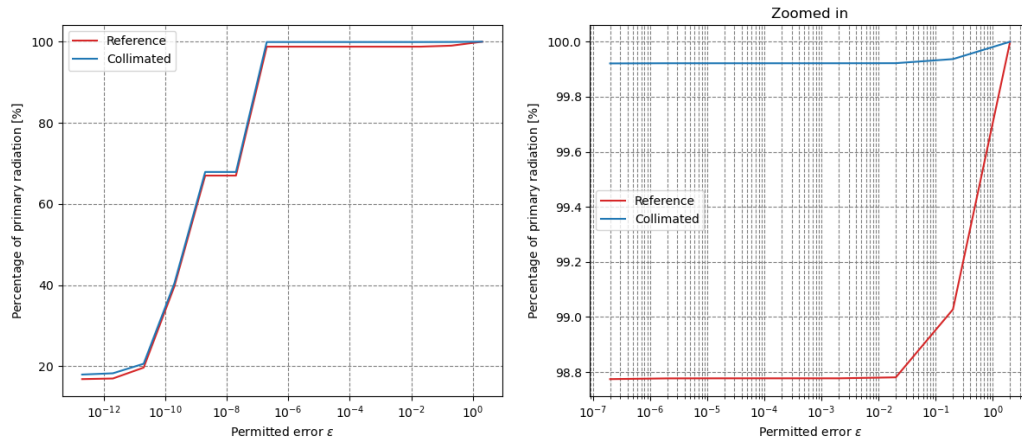
Figure 29. Graphs showing the percentage of radiation labeled primary passing through the exit plane of the collimator of both systems without and including the collimator, for a logarithmic decreasing permitted error ϵ. The right graph zooms in on the assumed constant region.

It was evident that for ϵ in the range of $2 \cdot 10^{-2}$ until $2 \cdot 10^{-7}$, the percentages of the primary radiation remained relatively stable, which is in line with the expected 7 decimal digit precision of 32-bit floats. The collimator reduced the permitted scattered radiation compared to the reference situation. This was presented in the higher percentage of primary photons leaving the exit plane of 99.22%, compared to the 98.77% in the reference situation. This was presumably due to the septa filtering out plenty of already scattered radiation, thus, further enhancing the imaging process.

5 | Discussion and Recommendation

5.1 Limited Cone Angle Review

As mentioned in the Methods, this work could only validate the designed collimator's efficacy on a substantially smaller FOV than what would be deemed realistic in practice due to computational limitations induced by GATE. The simulated cone angle C_α of 0.25 deg is only a fraction of the 13.7 deg that would be needed for a realistic simulation. A cluster with more memory available could simulate a larger C_α. However, for a realistic simulation, several terabytes of RAM would be needed, which is not feasible at this time. Therefore, the findings from the small FOV presented in this work must be extrapolated until clusters of the mentioned proportions become readily available, or the simulation approach needs to be significantly optimized by prospective work.

5.2 Practical Suitability

The simulations revealed promising results of using a collimator to virtually reduce the focal spot size to decrease the geometric unsharpness induced by the penumbra effect. Theoretically, the designed collimator was a reasonable alternative to entirely replacing the X-ray tube when a smaller focal spot is required. The collimator could be placed outside the X-ray tube, eliminating the need for changes to the tube and making it suitable for any existing system. However, the needed acquisition scaling factor of ~ 54 might introduce some difficulties in some instances. As mentioned, this scaling factor can be achieved by increasing the acquisition time and the tube current. It could be the case that it is not possible to sufficiently increase either of them to obtain the required scaling factor; a prolonged acquisition, including restrained movement of the subject, could be problematic, and the system may not be able to boost the tube current by a substantial factor. Therefore, comparable counts may not always be obtainable. The work by Muehllehner has shown that when the spatial resolution is increased in emission computed tomography, fewer counts may be needed to obtain similar image quality [115]. As the virtual reduced focal spot theoretically leads to an improved spatial resolution, the same principle could imply that the acquisition factor can be decreased significantly. Future work could be done to investigate what acquisition factor is required for acceptable image quality.

5.3 Gaussian Distributed Focal Spot

The geometry of the designed collimator acts like a Gaussian filter of the focal spot map. Using larger hole apertures, the design approach could generate a collimator

to convert the focal spot distribution to a 2D Gaussian while leaving the focal spot's physical shape unaltered, which is the case when the virtual focal spot width $\tilde{W}_{\text{VFS}}$ is greater or equal to the reference focal spot width W_{FS}, leading to

$$A_{\text{nom}} \geq \frac{W_{\text{FS}}}{\left(\frac{2F}{H} + 1\right)} \tag{21}$$

The larger hole apertures will naturally improve the total collimator sensitivity S and lower the required acquisition factor as more radiation is allowed to pass through. However, this is at the cost of not reducing the focal spot size. Even though the lack of focal spot size reduction will render this approach less effective, it could still be beneficial as it weighs emissions from the center more heavily, decreasing the penumbra effect caused by the off-center emissions. This could be a valuable middle-ground solution to the penumbra problem when a larger S is needed to minimize the acquisition factor in cases where such a factor can not be achieved.

5.4   Possible Design Improvements

Unfortunately, there was limited project time, so several possible improvements to the collimator's design could not be evaluated. As they might be interesting for potentially improved versions of the collimator, some of these suggestions will be discussed.

5.4.1   Moving Collimator

The septa of the collimator inherently all leave a so-called shadow on the measured projection, as discussed in the Literature section, which yields a shadow pattern on the projection. As the septa thicknesses in the proposed design are relatively exceptionally thin (~ 0.1 μm), this pattern is not presently visible in the projection. However, the pattern is theoretically still present in the projection, conceivably negatively impacting the signal-to-noise ratio. Therefore, a possible improvement to the collimator design is to lightly oscillate the collimator in the x-direction or define a position grid for the collimator movement as suggested by Beekman [1]. By doing so, the pattern will be nearly removed by spreading it across the projection. This could improve the signal-to-noise ratio and the image quality of the reconstruction that is devised from the projection.

5.4.2   Cone-Shaped Holes

Another suggestion is to use cone-shaped holes in the z-direction, along the collimator height H. As seen from figure 15, the combination of tilted holes and constant hole diameter along the z-direction produces an unnecessary thickness of the septa at the bottom of the collimator. The total collimator sensitivity S could increase significantly by using cone-shaped holes that would ensure a constant septal thickness, as off-center emissions depicted in figure 22 would be able to irradiate a larger area of the aperture. However, the design would need to be altered considerably,

as most of its theoretical derivations only hold for constant hole diameter. In addition, the collimator would lose its Gaussian filter behavior, which has proven to be a valuable asset. Nonetheless, finding the right balance between constant and cone-shaped holes could offer an improvement and would be an exciting approach for sequential research.

5.5   Impact on Reconstruction

Due to the mentioned work's time constraints, the collimator could only be tested on single projections, as a single projection took two days to complete. While the single projections already visibly revealed the effect of the virtual focal spot on the penumbra effect, the impact on the reconstruction is arguably of significantly greater value to the system's end-user. Future work could focus on validating the suggested image quality improvement due to the reduced virtual focal spot size by obtaining reconstructions from multiple projections. The spatial resolution of these reconstructions could offer a quantitative measure of the collimator's effectiveness and allow for objective comparisons between the virtual focal spot and similar techniques.

5.6   Feasibility of Production

The designed collimator included in this work comprised a total of 33,531 hexagon-shaped holes, with a nominal width A_{nom} of 1.08 µm, to cover a cone angle C_α of 0.25 degrees. A cone angle of 13.7 degrees was necessary to irradiate the whole detector plane, which is the standard in real acquisitions. The Python algorithm shows that in the case of 13.7 deg, the collimator must consist of 106,615,037 holes in the $12 \times 12 \times 5.5$ mm lead slab to cover such a cone angle. The question arises whether producing such a collimator satisfies the design criterion of being a practically viable alternative to entirely replacing the X-ray tube with a tube with a smaller focal spot. Based on the literature reviewed, there are no current methods to create consistent holes in these dimensions, especially considering the needed precision of their shape and hole angle. Any hypothetical method would also need an incredible hole creation rate; otherwise, the production process would be too time-consuming to make the collimators economically profitable compared to replacing the X-ray tube. Therefore, it can be concluded that even though collimation is a theoretical alternative, it is currently not feasible in practice. This could change due to newly established production methods in the future, potentially turning the theoretical principle into a viable, practical solution.

6 | Conclusion

This thesis aimed to validate Beekman's patent on how collimation could virtually reduce the focal spot size of an existing small-animal cone beam CT system to diminish the penumbra effect. After designing a collimator based on several initial criteria and validating the design by running Monte Carlo simulations, it was concluded that it is theoretically achievable to use collimation to virtually reduce the focal spot size to an arbitrarily chosen smaller virtual focal spot and significantly reduce the penumbra effect. The collimation-based focal spot reduction method proved suitable for existing CT systems, given that it could be mounted close to the X-ray tube window without requiring any integral changes to the X-ray tube. Furthermore, the results showed that the designed collimator acted as a Gaussian filter to the focal spot intensity map, which has additional benefits because it weighs center emissions more heavily than emissions from the edge of the virtual focal spot.

However, the collimator's practical suitability and production feasibility are quite problematic, as its total collimator sensitivity S was so low that an acquisition scaling factor of ~ 54 would be needed to obtain a similar amount of counts in the projection, which will not be feasible in every scenario. On top of that, a practically useful collimator would have to contain around 100 million holes in a 12×12 mm lead slab, which is probably impossible to manufacture currently. Future production techniques might facilitate the production of the collimator's theoretical geometry.

The collimator design could be further optimized to overcome these mentioned complications and make the collimator more viable. Sequential work building upon this thesis could focus on acquiring multiple projections using the virtual focal spot to reconstruct an image to validate the theoretically improved spatial resolution. The quantitative confirmation could further establish the theoretical effectiveness of focal spot collimation for future work to enhance reconstructions to uncover valuable information previously hidden.

A | Appendix

## A.1 'X-Ray Imaging Apparatus and Methods' Patent

This Appendix provides sections of Beekman's patent on collimation to reduce the focal spot size of existing X-ray systems. A more detailed description of the patent can be consulted at `https://patents.justia.com/patent/20220257205`.

A.1.1 Abstract

The X-ray imaging apparatus according to the invention may achieve one or more of the objectives because the collimator may serve as a means to select only a relatively small part of the X-ray source's focal spot. Ordinarily, such an X-ray source is an X-ray tube that has an emitting area with certain dimensions, the focal spot, that are not negligibly small with respect to the structures in the object to be examined, in particular the desired details thereof, and hence the resolution obtainable is often insufficient. An X-ray imaging apparatus for producing an X-ray image of an object, comprises a support frame in which an X-ray source and an X-ray detector are connected. The X-ray source and the X-ray detector define between them an object space for thc object to be examined. The X-ray source is configured to emit from a focal spot an X-ray beam with a main direction into the object space. The X-ray detector comprises an array of pixels sensitive to the X-ray radiation. The X-ray imaging apparatus further comprises a collimator arranged in proximity to the X-ray source and in the path of the X-ray beam between the X-ray source and the object to be examined. The collimator comprises one or more collimator bodies defining a plurality of passages of the collimator, the passages having respective central directions defining a common focal point of the collimator on the side of the X-ray source, preferably a 2D array of passages seen in a plane perpendicular to the main direction of thc X-ray beam. By using the inventive collimator arrangement, the apparent dimension(s) of the X-ray focal spot is (are) further reduced. In fact, the effective dimensions become close to the dimensions of the focal point or volume of the collimator. These dimensions, depending on the properties of the collimator, may in embodiments be limited to a small number of µm's for imaging of small animals, or a fraction of an mm for a clinical X-ray system or CT scanner.

A.1.2 Detailed Description Of Embodiments

The patent's diagrams are shown below. Based on the diagrams, a detailed description of the embodiments was provided.
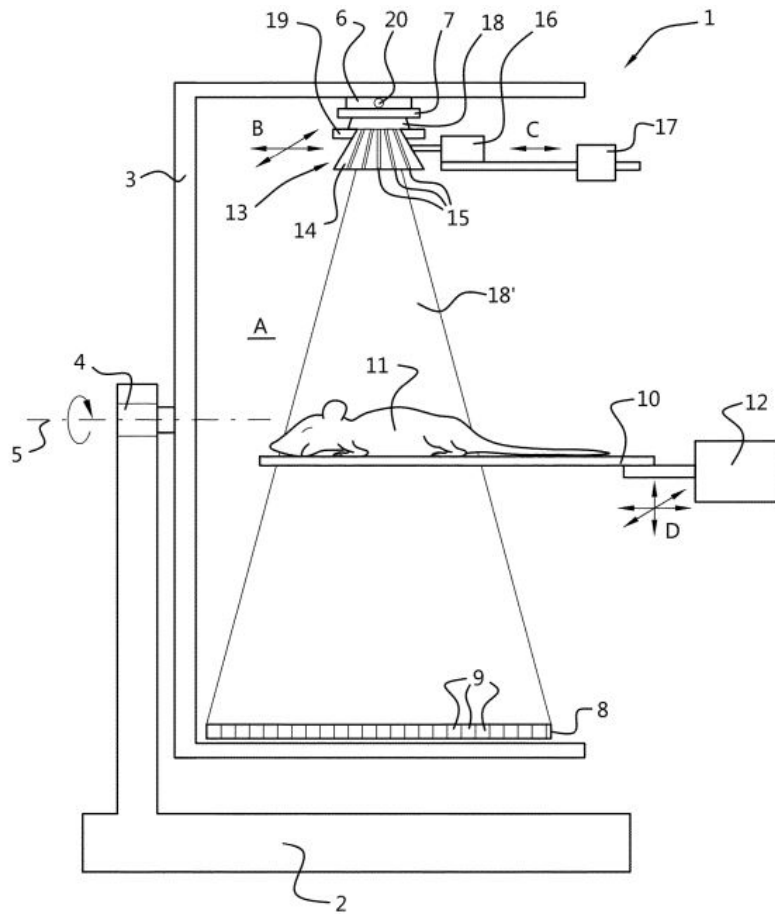
Figure 30. Diagram showing very diagrammatically a first embodiment of an X-ray imaging apparatus according to the invention, in a side elevational view [1].
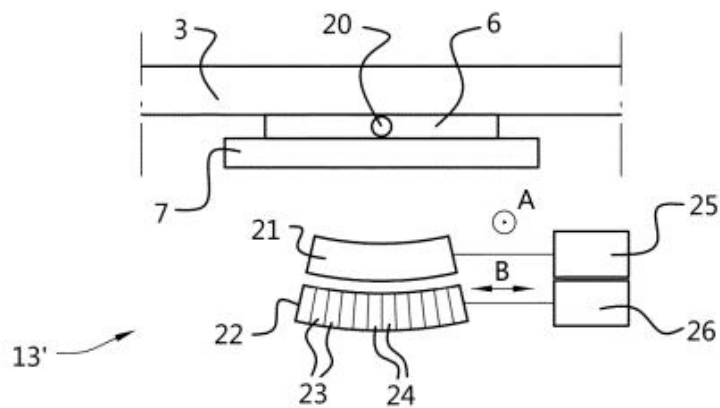
Figure 31. Diagram showing a very diagrammatical detail of a different embodiment of the X-ray imaging apparatus according to the invention [1].

Figure 30 shows very diagrammatically a first embodiment of an X-ray imaging
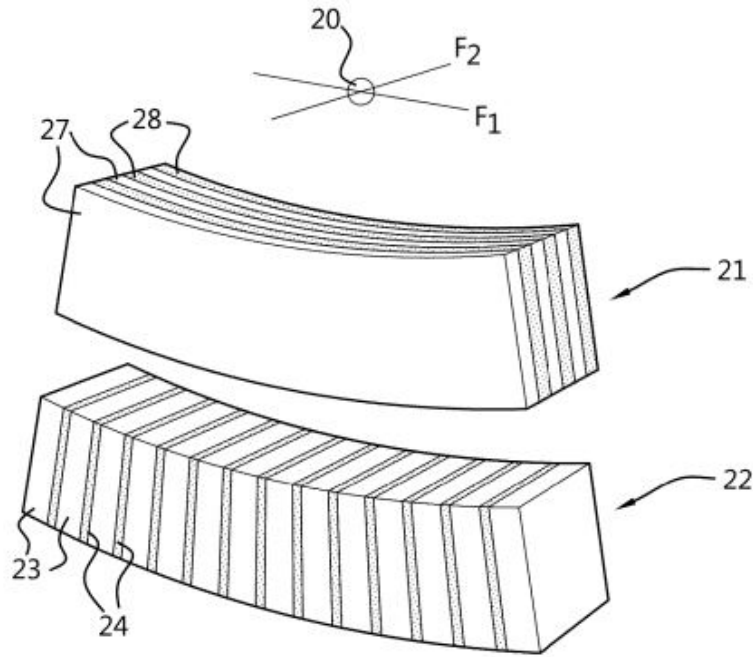
Figure 32. Diagram showing the collimator of Figure 2 in some more detail, in a diagrammatic perspective view [1].

apparatus 1 according to the invention, in a side elevational view.

The X-ray imaging apparatus 1 comprises a stationary main frame 2, to which is mounted a mobile, preferably rotatable support frame 3, e.g. embodied as a C-arm as shown here schematically, or embodied as a rotating gantry.

The support frame 3 is rotatable, preferably at least in a stepwise mode, by means of support frame rotator 4 around an axis 5, e.g. about a single axis, e.g. as in a gantry imaging system. In practical embodiments, the axis 5 is a horizontal axis.

An X-ray tube is indicated by reference numeral 6. Generally the X-ray tube 6 comprises an anode, an emitter arrangement comprising a cathode for emitting an electron beam towards the anode onto a focal spot on the anode, e.g. including electron optics for focusing the electron beam at the focal spot on the anode.

The X-ray tube 6 is provided with an X-ray window, e.g. a beryllium window 7.

An object carrier 10 is configured to carry an object 11 to be examined, e.g. a small animal, here a mouse.

An X-ray detector 8 is arranged for detecting at least part of the X-ray beam that has passed through the object 11.

Reference A indicates the object space between the X-ray tube 6 and the X-ray detector 8, wherein generally the object 11 to be examined is placed.

The X-ray detector 8 comprises an array, e.g. a 2D array, of pixels 9 sensitive to the

X-ray radiation.

For example, the object carrier 10 comprises a horizontal table on which an object 11 to be examined is placed.

Preferably, the object carrier 10 is movable by means of an associated object carrier mover 12, here a table mover 12, between a retracted position outside the object space A and an imaging position within the object space A.

Preferably, the object carrier 10 is movable by means of an associated object carrier mover 12, here a table mover 12, in one or more directions whilst the carrier 10 supports the object in the object space, e.g. in multiple orthogonal directions, e.g. in x, y, z directions, e.g. as indicated by arrows D. These one or more direction motions can be performed before, during and/or after scanning the object with the apparatus.

A computerized reconstructor reconstructs the imaging data and may, in embodiments, be configured to generate three dimensional (3D) volumetric image data indicative of an examination region and an object therein. The resulting volumetric image data can be processed by an image processor or the like to generate one or more images.

A general purpose computing system may be provided to serve as an operator console, and includes an output device such as a display and an input device such as a keyboard, mouse, and/or the like. Software resident on the console may allow the operator to control the operation of the imaging device, for example, allowing the operator to initiate scanning, etc.

In front of the window 7 there is provided a collimator 13, that has a collimator body 14 with through going passages 15, and which is movable in the direction of arrows B by collimator mover 16.

A collimator remover 17 may remove the collimator 13 from the emitted X-rays 18 in the direction of arrows C.

A beam shaping and blocking device is designated '19'.

A narrowed and more focused beam is indicated $18'$, while a focal point of the beam $18'$ is designated '20'.

In use, an object 11, such as a mouse or the like, is provided on the object carrier or table 10, and moved into the object space "A" by means of the table mover 12. By moving the table 10 in any one or more of the directions indicated by the arrows D, the object 11 may be positioned as desired with respect to the X-ray source 6 and the detector 8, i.e. with respect to the beam 18.

The X-rays 18 are generated by an X-ray source 6, in this case e.g. an X-ray tube, and emitted in a relatively coarse beam 18, for example with a size of its focal spot between about 0.1 and 1.2 mm diameter, depending on the properties of the source 6.

Using the inventive collimator, the coarse X-ray beam 18 emitted by the source 6 is trimmed down and shaped to a beam $18'$ that seems to originate from a much smaller effective focal spot defined by focal point or focal volume 20. This effective focal spot or volume could, for example, have a size of 20-25 µm diameter. Thereto, the coarse radiation 18 is sent through the collimator 13, with the collimator body 14 that has through going holes or passages 15.

In the example shown, the collimator is a cone beam collimator, in which there is one collimator body 14, and all holes or passages point to the same focal point on the focal spot 20.

Optionally, there is provided an additional beam shaping and blocking device 19, which is in principle not much more than a rim around the collimator body 14, that blocks any superficial radiation. The presence of such a simple rim, which may be as thick as the rest of the collimator body 14, ensures that there will be no X-rays apart from the ones in the beam $18'$, without having to provide too many holes 15 in the rim of the collimator body 14.

In use of the X-ray imaging apparatus 1, the collimator 13 may be moved with respect to the source 6 by means of the collimator mover 16, e.g. in the direction of the arrows B. Note that the collimator 13 need not be moved more than the centre-to-centre distance between the passages 15 in order to provide a full image.

To increase precision, it is preferred for the collimator 13 to be moved on an imaginary sphere around the focal point 20, such that the effective position of that focal point 20 remains the same during imaging. The collimator mover and control thereof should then of course be laid out correspondingly. This may be achieved by mechanical means or by adding movability in the third dimension and having the collimator mover 16 perform the desired combined spherical movement of the collimator 13, in casu of the collimator body 14.

The collimator mover 16 may comprise one or more piezo-actuators to provide for the movability. Such actuators can provide small required displacements with high precision, reliability and repetition frequency. Yet, other actuators are not excluded, such as stepper motors.

The collimator remover 17 is shown as being provided to remove the collimator 13 from the X-ray beam $18/18'$. In that case, the shaped beam $18'$ is then replaced again by the "coarse" X-rays 18, for example to image and examine much bigger objects 11, or with much higher intensity and correspondingly shorter exposure times. The collimator remover may comprise a coarser actuator than for the collimator mover 16, but it is also possible to combine the collimator mover and the collimator remover into one, such as with a device combining a piezo-actuator and a hinge or a linear actuator with a much larger stroke.

It is important to note that the drawing is not to scale. In particular, the dimensions of the object space A, that is, the distance between the X-ray tube 6 and the detector 8 are often between about 200 and 600 mm. Contrarily, the thickness of the collimator body 14 may in practice be about 1-2 mm. A larger thickness might

not improve the qualities any further, but would make it more difficult to make the holes or passages 15.

Also the number of passages 15 in the collimator body 14 will be (much) higher than the five shown here. The diameter of each of the passages 15 in reality will be a few µm, such as between 1 and 10 µm. Together, they ensure that the focal spot 20 of the X-ray tube 6 will effectively be reduced to a focal volume pf a few dozen µm, such as e.g. 25 µm across. Similarly, the pixels 9 of the X-ray detector 8 are often somewhat less than 0.1×0.1 mm, such as 75 µm×75 µm, their number correspondingly higher than shown in the drawing. In all cases, the numbers are exemplary, only giving an impression of realistic values.

Furthermore, while a whole mouse 11, or at least a large part of it, may be examined in the present situation, it is possible to bring the object 11 much closer to the X-ray source 6, the collimator 13 still being between the source 6 and the object 11. It will be so that often a correspondingly smaller object or part thereof may be examined. Because of the much larger magnification (ratio between "distance from source 6 to object 11" to "distance from source 6 to detector 8"), it becomes more important to have a high resolution in the image. This is possible with the present invention due to the provision of the collimator 13 between the source 6 and the object 11, which reduces the effective size (focal spot) of the X-ray source from, say, 0.1 to 2 mm to, say, 25 µm. Note that, when bringing the object 11 closer to the source 6, it may be necessary to adapt the way in which the frame 3 with source 6 and detector 8 is rotated around an axis through the object 11, in order to obtain sufficient angular information. This adaptation may comprise sliding the support frame 3 in a direction perpendicular to the direction of the axis 5, such that the X-ray source 6 comes much closer to the axis 5 than the detector 8. Any other measure that achieves the same effect is also possible here.

The support frame 3 is here shown to be rotatable with respect to the main frame 2, e.g. about a horizontal rotation axis. However, it is also possible to have a fixed frame 3 without the rotatability, and have the object carrier 10 rotate with respect to the frame 3, or even have no rotation at all and have only 2D imaging properties.

Figure 31 shows a very diagrammatical detail of a different embodiment of the X-ray imaging apparatus according to the invention, in particular the part with the X-ray source and the collimator. Herein, as in all of the drawing, similar parts are denoted by the same reference numerals.

The detail shows a small part of the frame 3 with an X-ray source 6, a protective but X-ray transparent window 7, and a different collimator $13'$ having focal point 20 on the focal spot of the X-ray source 6.

The collimator $13'$ comprises a set of a first collimator body 21 and a second collimator body 22 that is arranged in series with the first collimator body 21. The first collimator body 21 comprises a first stack of spaced apart first plates 26 with respective first slit spaces 28 between adjacent plates. These first slit spaces 28 are all directed towards a common first imaginary line F1. The second collimator body 22 comprises a second stack of spaced apart second plates 23 with respective second

slit spaces 24 there between. These second slit spaces 24 are all directed towards a common second imaginary line F2. The plates of the bodies are non-parallel from the one body to the other body, so that the first and second common imaginary lines cross one another in the common focal point 20. As a result the first and second slit spaces 28, 24 together form the plurality of passages of the collimator $13'$ focused on the common focal point 20, e.g. of very small size, e.g. much smaller than the focal spot of the X-ray source in absence of the collimator $13'$.

The bodies 21, 22 may be moved by a corresponding mover 25, 26 about the respective focal line.

The bodies 21, 22 may interface with curved or even spherical adjoining sides as schematically illustrated, e.g. allowing for motion of each body about the respective focal line, e.g. by a corresponding mover 25, 26.

Figure 32 shows the collimator $13'$ in some more detail, in a diagrammatic perspective view.

When the beam of X-rays from the X-ray source 6 of figure 31 shines through this collimator $13'$, the resulting source as "seen" by an object is again an apparent focal spot 20, where the focal lines F1 and F2 cross.

The numbers of plates shown here by way of example is arbitrary, and these numbers, as well as the thickness of the plates 27, 23 and the width of the slits 28, 24 may be selected as desired.

The first collimator body mover 25 is arranged to move the first body 21, e.g. in a direction substantially perpendicular to the main direction of the corresponding slits 28, albeit in particular as preferred on a sphere around the focal point 20 or about line F1, i.e. the direction indicated by "A" in figure 31, which is into/out of the paper. Similarly, the second collimator body mover 26 may be arranged to move the second body 22 in the perpendicular direction of arrow B.

The movements of the two bodies 21, 22 may be coordinated, such as moving the first body 21 over a first step, and then performing a sweeping or further step like motion for the second body 22, or vice versa. Faster vibrating movements of both bodies 21, 22 during imaging are also possible, as long as all desired or possible beam directions originating from the focal point are imaged sufficiently. Note that the first and second collimator body movers may again comprise a piezo-actuator or the like, and may together be complemented by a collimator remover (not shown) for removing the collimator $13'$, likewise as for the collimator remover 17 as per figure 30.

The embodiments and figures are only given as an exemplifying explanation of the invention, without limiting the scope of the appended claims.

Bibliography

[1] F. J. Beekman. (MILabs B.V.). X-Ray Imaging Apparatus And Methods, 2021. Patent by World Intellectual Property Organiziation (PCT/EP2020/072-114). Filed on 10-08-2020. URL `https://patents.justia.com/patent/20220257205`. Accessed on 29-01-2023.

[2] R. A. Schulz, J. A. Stein, and N. J. Pelc. How CT happened: the early development of medical computed tomography. *J Med Imaging (Bellingham)*, 8(5):052110, 2021. ISSN 2329-4302. doi: 10.1117/1.Jmi.8.5.052110.

[3] G. van Kaick and S. Delorme. Computed tomography in fields outside medicine. *European Radiology*, 15 Suppl 4:D74–81, 2005. doi: 10.1007/s10406-005-0138-1.

[4] M. Vicente, J. Minguez, and D. Cabrera. *The Use of Computed Tomography to Explore the Microstructure of Materials in Civil Engineering: From Rocks to Concrete.* 2017. ISBN 978-953-51-3367-4. doi: 10.5772/intechopen.69245.

[5] M. Yester and G. Barnes. *Geometrical Limitations Of Computed Tomography (CT) Scanner Resolution*, volume 127 of *Application of Optical Instrumentation in Medicine VI.* SPIE, 1977.

[6] J. Wang and D. Fleischmann. Improving Spatial Resolution at CT: Development, Benefits, and Pitfalls. *Radiology*, 289(1):261–262, 2018. ISSN 0033-8419. doi: 10.1148/radiol.2018181156.

[7] K. Holmes, M. Elkington, and P. Harris. *Clark's Essential Physics in Imaging for Radiographers.* CRC Press, first edition, 2013. ISBN 9781444165036. doi: 10.1201/b15383.

[8] P. Suetens. *Fundamentals of Medical Imaging.* Cambridge University Press, Cambridge, second edition, 2009. doi: 10.1017/CBO9780511596803.

[9] P. Russo. *Physical Basis of X-Ray Imaging*, pages 1–48. First edition, 2014. ISBN 9780444536334. doi: 10.1016/B978-0-444-53632-7.00201-X.

[10] F. E. Zink. X-ray tubes. *Radiographics*, 17(5):1259–68, 1997. ISSN 0271-5333 (Print) 0271-5333. doi: 10.1148/radiographics.17.5.9308113.

[11] S. Dushman. Thermionic Emission. *Reviews of Modern Physics*, 2(4):381–476, 1930. doi: 10.1103/RevModPhys.2.381.

[12] P. T. McCarthy, R. G. Reifenberger, and T. S. Fisher. Thermionic and Photo-Excited Electron Emission for Energy-Conversion Processes. *Frontiers in Energy Research*, 2, 2014. ISSN 2296-598X. doi: 10.3389/fenrg.2014.00054.

[13] P. Lang and B. Smith. Ionization Energies of Atoms and Atomic Ions. *Journal of Chemical Education - J CHEM EDUC*, 80, 2003. doi: 10.1021/ed080p938.

[14] PhysicsOpenLab. X-Ray Emission, 2018. URL https://physicsopenlab.org/2018/02/13/x-ray-emission/. Accessed on June 30, 2022.

[15] E. Ammann and W. Kutschera. X-ray tubes–continuous innovative technology. *The British Journal of Radiology*, 70 Spec No:S1–9, 1997. ISSN 0007-1285 (Print) 0007-1285. doi: 10.1259/bjr.1997.0002.

[16] M. Taubin, D. Chesnokov, and A. Pavlov. Cathodes for medical purpose X-ray tubes. *Journal of Physics: Conference Series*, 808:012004, 2017. doi: 10.1088/1742-6596/808/1/012004.

[17] J. Shultis and R. Faw. Radiation shielding technology. *Health physics*, 88: 587–612, 2005. doi: 10.1097/01.HP.0000148615.73825.b1.

[18] Z. Li, W. Zhou, Xi. Zhang, Y. Gao, and S. Guo. High-efficiency, flexibility and lead-free X-ray shielding multilayered polymer composites: layered structure design and shielding mechanism. *Scientific Reports*, 11(1):4384, 2021. ISSN 2045-2322. doi: 10.1038/s41598-021-83031-4.

[19] W. B. Nottingham. Thermionic Emission from Tungsten and Thoriated Tungsten Filaments. *Physical Review*, 49(1):78–97, 1936. doi: 10.1103/PhysRev.49.78.

[20] G. B. van der Voet, T. I. Todorov, J. A. Centeno, W. Jonas, J. Ives, and F. G. Mullick. Metals and health: a clinical toxicological perspective on tungsten and review of the literature. *Mil Med*, 172(9):1002–5, 2007. ISSN 0026-4075 (Print) 0026-4075. doi: 10.7205/milmed.172.9.1002.

[21] P. Schardt, J. Deuringer, J. Freudenberger, E. Hell, W. Knüpfer, D. Mattern, and M. Schild. New x-ray tube performance in computed tomography by introducing the rotating envelope tube technology. *Medical Physics*, 31(9): 2699–706, 2004. ISSN 0094-2405 (Print) 0094-2405. doi: 10.1118/1.1783552.

[22] E. M. Savitskii, M. A. Tylkina, S. I. Ipatova, and E. I. Pavlova. Properties of tungsten-rhenium alloys. *Metal Science and Heat Treatment of Metals*, 2(9): 483–486, 1960. ISSN 1573-8973. doi: 10.1007/BF00649725.

[23] J. M. Boone, T. R. Fewell, and R. J. Jennings. Molybdenum, rhodium, and tungsten anode spectral models using interpolating polynomials with application to mammography. *Medical Physics*, 24(12):1863–1874, 1997. ISSN 0094-2405. doi: 10.1118/1.598100.

[24] L. W. Goldman. Principles of CT: Multislice CT. *Journal of Nuclear Medicine Technology*, 36(2):57–68, 2008. doi: 10.2967/jnmt.107.044826.

[25] C. Ronda, H. Wieczorek, V. Khanin, and P. Rodnyi. Review—Scintillators for Medical Imaging: A Tutorial Overview. *ECS Journal of Solid State Science*

and Technology, 5(1):R3121–R3125, 2015. ISSN 2162-8769 2162-8777. doi: 10.1149/2.0131601jss.

[26] J. Hsieh and T. Flohr. Computed tomography recent history and future perspectives. *Journal of Medical Imaging*, 8(5):052109, 2021. doi: 10.1117/1.JMI.8.5.052109.

[27] L. W. Goldman. Principles of CT and CT Technology. *Journal of Nuclear Medicine Technology*, 35(3):115–128, 2007. doi: 10.2967/jnmt.107.042978.

[28] W. Stiller. Basics of iterative reconstruction methods in computed tomography: A vendor-independent overview. *European Journal of Radiology*, 109: 147–154, 2018. ISSN 0720-048X. doi: 10.1016/j.ejrad.2018.10.025.

[29] M. J. Willemink and P. B. Noël. The evolution of image reconstruction for CT—from filtered back projection to artificial intelligence. *European Radiology*, 29(5):2185–2195, 2019. ISSN 1432-1084. doi: 10.1007/s00330-018-5810-7.

[30] W. A. Kalender. X-ray computed tomography. *Physics in Medicine and Biology*, 51(13):R29–R43, 2006. ISSN 0031-9155 1361-6560. doi: 10.1088/0031-9155/51/13/r03.

[31] K. Nieman, A. Coenen, and M. Dijkshoorn. *5 - Computed tomography*, pages 97–125. Woodhead Publishing, 2015. ISBN 978-1-78242-282-2. doi: 10.1016/B978-1-78242-282-2.00005-6.

[32] E. Lin and A. Alessio. What are the basic concepts of temporal, contrast, and spatial resolution in cardiac CT? *Journal of Cardiovascular Computed Tomography*, 3(6):403–408, 2009. ISSN 1876-861X 1934-5925. doi: 10.1016/j.jcct.2009.07.003.

[33] F. R. Verdun, D. Racine, J. G. Ott, M. J. Tapiovaara, P. Toroi, F. O. Bochud, W. J. H. Veldkamp, A. Schegerer, R. W. Bouwman, I. Hernandez Giron, N. W. Marshall, and S. Edyvean. Image quality in CT: From physical measurements to model observers. *Physica Medica*, 31(8):823–843, 2015. ISSN 1120-1797. doi: 10.1016/j.ejmp.2015.08.007.

[34] A. Staude and J. G. Bam. Determining the Spatial Resolution in Computed Tomography – Comparison of MTF and Line-Pair Structures. 2011.

[35] A. L. C. Kwan, J. M. Boone, K. Yang, and S. Huang. Evaluation of the spatial resolution characteristics of a cone-beam breast CT scanner. *Medical Physics*, 34(1):275–281, 2007. ISSN 0094-2405. doi: 10.1118/1.2400830.

[36] A. du Plessis, S. G. le Roux, and A. Guelpa. Comparison of medical and industrial X-ray computed tomography for non-destructive testing. *Case Studies in Nondestructive Testing and Evaluation*, 6:17–25, 2016. ISSN 2214-6571. doi: 10.1016/j.csndt.2016.07.001.

[37] A. du Plessis, C. Broeckhoven, A. Guelpa, and S. G. le Roux. Laboratory x-ray micro-computed tomography: a user guideline for biological samples. *Gigascience*, 6(6):1–11, 2017. ISSN 2047-217x. doi: 10.1093/gigascience/gix027.

[38] H. J. Haugen, S. B. Qasim, J. P. Matinlinna, P. Vallittu, and L. P. Nogueira. Nano-CT as tool for characterization of dental resin composites. *Scientific Reports*, 10(1):15520, 2020. ISSN 2045-2322. doi: 10.1038/s41598-020-72599-y.

[39] D. J. Goodenough and K. E. Weaver. Factors related to low contrast resolution in CT scanners. *Computerized Radiology*, 8(5):297–308, 1984. ISSN 0730-4862. doi: 10.1016/0730-4862(84)90042-8.

[40] H. Alsleem and R. Davidson. Factors Affecting Contrast-Detail Performance in Computed Tomography: A Review. *Journal of Medical Imaging and Radiation Sciences*, 44:62–70, 2013. doi: 10.1016/j.jmir.2012.12.001.

[41] K. Juluru, J. C. Shih, A. Raj, J. P. Comunale, H. Delaney, E. D. Greenberg, C. Hermann, Y. B. Liu, A. Hoelscher, N. Al-Khori, and P. C. Sanelli. Effects of increased image noise on image quality and quantitative interpretation in brain CT perfusion. *American Journal of Neuroradiology*, 34(8):1506–1512, 2013. ISSN 1936-959X 0195-6108. doi: 10.3174/ajnr.A3448.

[42] M. Diwakar and M. Kumar. A review on CT image noise and its denoising. *Biomedical Signal Processing and Control*, 42:73–88, 2018. ISSN 1746-8094. doi: 10.1016/j.bspc.2018.01.010.

[43] A. Rodriguez-Molares, O. M. Hoel Rindal, J. D'hooge, S. Masoy, A. Austeng, and H. Torp. The Generalized Contrast-to-Noise Ratio. In *2018 IEEE International Ultrasonics Symposium (IUS)*, pages 1–4, 2018. ISBN 1948-5727. doi: 10.1109/ULTSYM.2018.8580101.

[44] M. Cohnen, H. Fischer, J. Hamacher, E. Lins, R. Kötter, and U. Mödder. CT of the Head by Use of Reduced Current and Kilovoltage: Relationship between Image Quality and Dose Reduction. *American Journal of Neuroradiology*, 21 (9):1654–1660, 2000.

[45] M. McNitt-Gray. Tradeoffs in CT Image Quality and Dose. *Medical Physics*, 33, 2006.

[46] J. A. Seibert. Tradeoffs between image quality and dose. *Pediatr Radiol*, 34 Suppl 3:S183–95; discussion S234–41, 2004. ISSN 0301-0449 (Print) 0301-0449. doi: 10.1007/s00247-004-1268-7.

[47] T. S. Curry, J. E. Dowdey, and R. C. Murry. *Christensen's Physics of Diagnostic Radiology*. Lea & Febiger, 1990. ISBN 9780812113105.

[48] S. C. Bushong. *Radiologic Science for Technologists - E-Book: Physics, Biology, and Protection*. Elsevier Health Sciences, 2013. ISBN 9780323292078.

[49] P. M. Andrus and A. Hambleton. The Capacity of X-ray Tubes as Influenced by the Geometric Design of the Focal Spot, Including the Advantages and Limitations of the Line Focus Principle. *Radiology*, 18(3):521–531, 1932. doi: 10.1148/18.3.521.

[50] R. Percuoco. *Chapter 1 - Plain Radiographic Imaging*, pages 1–43. Mosby,

Saint Louis, 2014. ISBN 978-0-323-08495-6. doi: 10.1016/B978-0-323-08495-6.00001-4.

[51] B. Kim and J. Baek. *The effect of a finite focal spot size on location dependent detectability in a fan beam CT system*, volume 10132 of *SPIE Medical Imaging*. SPIE, 2017.

[52] S. E. Smith. *Conventional radiography and computed tomography*, book section 40, pages 307–321. Mosby, Philadelphia, sixth edition, 2015. ISBN 978-0-323-09138-1. doi: 10.1016/B978-0-323-09138-1.00040-1.

[53] H. Arabi, A. Kamali-Asl, and S. M. R. Aghamiri. The effect of focal spot size on the spatial resolution of variable resolution X-ray CT scanner. *Iranian Journal of Radiation Research*, 8, 2010.

[54] F. Nachtrab, T. Ebensperger, B. Schummer, F. Sukowski, and R. Hanke. Laboratory X-ray microscopy with a nano-focus X-ray source. *Journal of Instrumentation*, 6:C11017, 2011. doi: 10.1088/1748-0221/6/11/C11017.

[55] A. Robinson and G. M. Grimshaw. Measurement of the focal spot size of diagnostic X-ray tubes—a comparison of pinhole and resolution methods. *The British Journal of Radiology*, 48(571):572–580, 1975. doi: 10.1259/0007-1285-48-571-572.

[56] J. D. Everson and J. E. Gray. Focal-spot measurement: comparison of slit, pinhole, and star resolution pattern techniques. *Radiology*, 165(1):261–264, 1987. doi: 10.1148/radiology.165.1.3628780.

[57] K. Bavendiek, U. Ewert, A. Riedo, U. Heike, and U. Zscherpel. New measurement methods of focal spot size and shape of X-ray tubes in digital radiological applications in comparison to current standards. In *18th World Conference on Nondestructive Testing*, pages 16–20. Citeseer, 2012.

[58] K. Doi, L. N. Loo, and H. P. Chan. X-ray tube focal spot sizes: comprehensive studies of their measurement and effect of measured size in angiography. *Radiology*, 144(2):383–93, 1982. ISSN 0033-8419 (Print) 0033-8419. doi: 10.1148/radiology.144.2.7089295.

[59] I. Grabska, E. Fabiszewska, K. Pasicz, and W. Skrzyński. Estimation of the effective focal spot sizes in medical diagnostic X-ray tube assemblies. *Polish Journal of Medical Physics and Engineering*, 22(2):25–33, 2016. doi: doi:10.1515/pjmpe-2016-0006.

[60] A. Jain, A. Panse, D. R. Bednarek, and S. Rudin. Focal spot measurements using a digital flat panel detector. *Proc SPIE Int Soc Opt Eng*, 9033(90335f), 2014. ISSN 0277-786X (Print) 0277-786x. doi: 10.1117/12.2043057.

[61] P. Spiegler and W. C. Breckinridge. Imaging of Focal Spots by Means of the Star Test Pattern. *Radiology*, 102(3):679–685, 1972. doi: 10.1148/102.3.679.

[62] E. Milne and W. Roeck. *Determinants and Indices of Focal Spot Performance*

-*The Concept of Three-Dimensionality*, volume 0056 of *Medical X-Ray Photo-Optical Systems Evaluation*. SPIE, 1974.

[63] X. J. Rong, K. T. Krugh, S. J. Shepard, and W. R. Geiser. Measurement of focal spot size with slit camera using computed radiography and flat-panel based digital detectors. *Medical Physics*, 30(7):1768–75, 2003. ISSN 0094-2405 (Print) 0094-2405. doi: 10.1118/1.1579583.

[64] M. Nishiki, S. Yanagita, N. Nishikawa, and H. Sugimura. Measurement of the x-ray effective focal spot size with edge response analysis using digital detectors. *J Med Imaging (Bellingham)*, 7(2):023502, 2020. ISSN 2329-4302 (Print) 2329-4302. doi: 10.1117/1.Jmi.7.2.023502.

[65] X. Duan, J. Grimes, L. Yu, S. Leng, and C. McCollough. The Influence of Tube Current On X-Ray Focal Spot Size for 70 KV CT Imaging. *Medical Physics*, 41:559–559, 2014. doi: 10.1118/1.4889634.

[66] J. Grimes, X. Duan, L. Yu, A. F. Halaweish, N. Haag, S. Leng, and C. McCollough. The influence of focal spot blooming on high-contrast spatial resolution in CT imaging. *Medical Physics*, 42(10):6011–20, 2015. ISSN 0094-2405. doi: 10.1118/1.4931053.

[67] T. Wood. An introduction to radiography with X-rays and the X-ray tube, 2015. URL https://slidetodoc.com/frcr-physics-lectures-diagnostic-radiolo.. Accessed on June 30, 2022.

[68] S. Mori, M. Endo, K. Nishizawa, M. Ohno, H. Miyazaki, K. Tsujita, and Y. Saito. Prototype heel effect compensation filter for cone-beam CT. *Physics in Medicine and Biology*, 50(22):N359–70, 2005. ISSN 0031-9155 (Print) 0031-9155. doi: 10.1088/0031-9155/50/22/n02.

[69] M. Z. do Nascimento, A. F. Frére, and F. Germano. An automatic correction method for the heel effect in digitized mammography images. *J Digit Imaging*, 21(2):177–87, 2008. ISSN 0897-1889 (Print) 0897-1889. doi: 10.1007/s10278-007-9072-1.

[70] M. W. Kusk, J. M. Jensen, E. H. Gram, J. Nielsen, and H. Precht. Anode heel effect: Does it impact image quality in digital radiography? A systematic literature review. *Radiography (Lond)*, 27(3):976–981, 2021. ISSN 1078-8174. doi: 10.1016/j.radi.2021.02.014.

[71] S. Gorham and P. Brennan. Impact of focal spot size on radiologic image quality: A visual grading analysis. *Radiography*, 16:304–313, 2010. doi: 10.1016/j.radi.2010.02.007.

[72] W. Kei Ma, P. Hogg, and S. Norton. Effects of kilovoltage, milliampere seconds, and focal spot size on image quality. *Radiol Technol*, 85(5):479–85, 2014. ISSN 0033-8397.

[73] R. Mikayama, T. Shirasaka, H. Yabuuchi, Y. Sakai, T. Kojima, M. Kondo, H. Yoshikawa, and T. Kato. Effect of scan mode and focal spot size in airway

dimension measurements for ultra-high-resolution computed tomography of chronic obstructive pulmonary disease: A COPDGene phantom study. *Physica Medica*, 70:102–108, 2020. ISSN 1120-1797. doi: 10.1016/j.ejmp.2019.12.025.

[74] L. J. Oostveen, K. L. Boedeker, M. Brink, M. Prokop, F. de Lange, and I. Sechopoulos. Physical evaluation of an ultra-high-resolution CT scanner. *European Radiology*, 30(5):2552–2560, 2020. ISSN 1432-1084. doi: 10.1007/s00330-019-06635-5.

[75] A. E. Papadakis and J. Damilakis. The effect of tube focal spot size and acquisition mode on task-based image quality performance of a GE revolution HD dual energy CT scanner. *Phys Med*, 86:75–81, 2021. ISSN 1120-1797. doi: 10.1016/j.ejmp.2021.05.025.

[76] E. L. Nickoloff, E. Donnelly, L. Eve, J. V. Atherton, and T. Asch. Mammographic resolution: Influence of focal spot intensity distribution and geometry. *Medical Physics*, 17(3):436–447, 1990. ISSN 0094-2405. doi: 10.1118/1.596482.

[77] F. Ouandji, E. Potter, W. Chen, and H. Liu. *Impact of focal spot size on the spatial resolution of a digital x-ray imaging system for small-animal studies*, volume 4615 of *International Symposium on Biomedical Optics*. SPIE, 2002. doi: 10.1117/12.466639.

[78] J. Rueckel, M. Stockmar, F. Pfeiffer, and J. Herzen. Spatial resolution characterization of a X-ray microCT system. *Applied Radiation and Isotopes*, 94: 230–234, 2014. ISSN 0969-8043. doi: 10.1016/j.apradiso.2014.08.014.

[79] P. Forthmann, T. Köhler, P. G. C. Begemann, and M. Defrise. Penalized maximum-likelihood sinogram restoration for dual focal spot computed tomography. *Physics in Medicine and Biology*, 52(15):4513–4523, 2007. ISSN 0031-9155 1361-6560. doi: 10.1088/0031-9155/52/15/010.

[80] A. Astolfo, I. Buchanan, T. Partridge, G. K. Kallon, C. K. Hagen, P. R. T. Munro, M. Endrizzi, D. Bate, and A. Olivo. The effect of a variable focal spot size on the contrast channels retrieved in edge-illumination X-ray phase contrast imaging. *Scientific Reports*, 12(1):3354, 2022. ISSN 2045-2322. doi: 10.1038/s41598-022-07376-0.

[81] X. Hu, Y. Zhong, Y. Huang, C. Shen, and X. Jia. Improving small animal cone beam CT resolution by mitigating x-ray focal spot induced blurring via deconvolution. *Physics in Medicine and Biology*, 67(12):125005, 2022. ISSN 0031-9155 1361-6560. doi: 10.1088/1361-6560/ac6b7a.

[82] M. Chang, Y. Xiao, and Z. Chen. Improve spatial resolution by Modeling Finite Focal Spot (MFFS) for industrial CT reconstruction. *Opt Express*, 22 (25):30641–56, 2014. ISSN 1094-4087. doi: 10.1364/oe.22.030641.

[83] P. Lillaney, M. Shin, W. Hinshaw, and R. Fahrig. Electrostatic focal spot correction for x-ray tubes operating in strong magnetic fields. *Medical Physics*, 41(11):112302, 2016. ISSN 0094-2405. doi: 10.1118/1.4898099.

[84] M. F. Kijewski. *Positron Emission Tomography (PET) and Single-Photon Emission Computed Tomography (SPECT) Physics*, book section 32, pages 353–358. Academic Press, San Diego, 2016. ISBN 978-0-12-800945-1. doi: 10.1016/B978-0-12-800945-1.00032-X.

[85] M. Sandborg, D. R. Dance, G. A. Carlsson, and J. Persliden. Selection of anti-scatter grids for different imaging tasks: the advantage of low atomic number cover and interspace materials. *The British Journal of Radiology*, 66(792): 1151–63, 1993. ISSN 0007-1285. doi: 10.1259/0007-1285-66-792-1151.

[86] K. Van Audenhaege, R. Van Holen, S. Vandenberghe, C. Vanhove, S. D. Metzler, and S. C. Moore. Review of SPECT collimator selection, optimization, and fabrication for clinical and preclinical imaging. *Medical Physics*, 42(8): 4796–813, 2015. ISSN 0094-2405. doi: 10.1118/1.4927061.

[87] J. J. Lifton, A. A. Malcolm, and J. W. McBride. An experimental study on the influence of scatter and beam hardening in x-ray CT for dimensional metrology. *Measurement Science and Technology*, 27(1):015007, 2015. ISSN 0957-0233 1361-6501. doi: 10.1088/0957-0233/27/1/015007.

[88] G. Muehllehner, J. Dudek, and R. Moyer. Influence of hole shape on collimator performance. *Physics in Medicine and Biology*, 21(2):242–50, 1976. ISSN 0031-9155. doi: 10.1088/0031-9155/21/2/006.

[89] C. Beijst, M. Elschot, M. A. Viergever, and H. W. A. M. de Jong. A Parallel-Cone Collimator for High-Energy SPECT. *Journal of Nuclear Medicine*, 56 (3):476–482, 2015. doi: 10.2967/jnumed.114.149658.

[90] M. F. Smith, R. J. Jaszczak, and H. Wang. Pinhole aperture design for /sup 131/I tumor imaging. *IEEE Transactions on Nuclear Science*, 44(3):1154–1160, 1997. ISSN 1558-1578. doi: 10.1109/23.596980.

[91] M. C. Goorden and F. J. Beekman. High-resolution tomography of positron emitters with clustered pinhole SPECT. *Physics in Medicine and Biology*, 55 (5):1265–77, 2010. ISSN 0031-9155. doi: 10.1088/0031-9155/55/5/001.

[92] J. Lin and S. R. Meikle. SPECT using asymmetric pinholes with truncated projections. *Physics in Medicine and Biology*, 56(13):4103–18, 2011. ISSN 0031-9155. doi: 10.1088/0031-9155/56/13/023.

[93] J. Pirayesh Islamian, A. Azazrm, B. Mahmoudian, and E. Gharepapagh. Advances in Pinhole and Multi-Pinhole Collimators For Single Photon Emission Computed Tomography Imaging. *World Journal of Nuclear Medicine*, 14:3–9, 2015. doi: 10.4103/1450-1147.150505.

[94] J. A. Sorenson and M. E. Phelps. *Physics in nuclear medicine Second edition*. Grune and Stratton Inc, United States, second edition, 1987. ISBN 0-8089-1804-4.

[95] E. L. Keller. Optimum dimensions of parallel-hole, multi-aperture collimators for gamma-ray cameras. *Journal of Nuclear Medicine Technology*, 9(6):233–5, 1968. ISSN 0161-5505.

[96] G. L. Zeng, J. R. Galt, M. N. Wernick, R. A. Mintzer, and J. N. Aarsvold. *Single-Photon Emission Computed Tomography*, book section 7, pages 127–152. Academic Press, San Diego, 2004. ISBN 978-0-12-744482-6. doi: 10.1016/B978-012744482-6.50010-7.

[97] V. Bom, M. Goorden, and F. Beekman. Comparison of pinhole collimator materials based on sensitivity equivalence. *Physics in Medicine and Biology*, 56(11):3199–214, 2011. ISSN 0031-9155. doi: 10.1088/0031-9155/56/11/003.

[98] M. P. Nguyen, M. C. Goorden, C. Kamphuis, and F. J. Beekman. Evaluation of pinhole collimator materials for micron-resolution <i>ex vivo</i> SPECT. *Physics in Medicine and Biology*, 64(10):105017, 2019. ISSN 1361-6560. doi: 10.1088/1361-6560/ab1618.

[99] O. Makarova, G. Yang, P. Amstutz, and C. Tang. Fabrication of antiscatter grids and collimators for X-ray and gamma-ray imaging by lithography and electroforming. *Microsystem Technologies*, 14:1613–1619, 2008. doi: 10.1007/s00542-008-0558-7.

[100] K. W. LaBarge. Electrical discharge machining. *J Dent Technol*, 14(9):19–22, 1997. ISSN 1088-3118 (Print) 1088-3118.

[101] K. Deprez, S. Vandenberghe, K. Van Audenhaege, J. Van Vaerenbergh, and R. Van Holen. Rapid additive manufacturing of MR compatible multipinhole collimators with selective laser melting of tungsten powder. *Medical Physics*, 40(1):012501, 2013. ISSN 0094-2405. doi: 10.1118/1.4769122.

[102] K. Deprez. *Preclinical SPECT imaging based on compact collimators and high resolution scintillation detectors*. PHD Thesis, Ghent University, 2014.

[103] J. H. Siewerdsen, D. J. Moseley, B. Bakhtiar, S. Richard, and D. A. Jaffray. The influence of antiscatter grids on soft-tissue detectability in cone-beam computed tomography with flat-panel detectors. *Medical Physics*, 31 (12):3506–3520, 2004. ISSN 0094-2405. doi: 10.1118/1.1819789.

[104] J. H. Siewerdsen, M. J. Daly, B. Bakhtiar, D. J. Moseley, S. Richard, H. Keller, and D. A. Jaffray. A simple, direct method for x-ray scatter estimation and correction in digital radiography and cone-beam CT. *Medical Physics*, 33(1): 187–97, 2006.

[105] O. S. Huey, Y. J. See, S. Nabila, H. S. Ping, and I. Suzanah. Collimator and energy window optimization for practical imaging protocol and quantification of Yttrium-90 bremsstrahlung spect/ct: A phantom study. *Radiation Physics and Chemistry*, 178:109080, 2021. ISSN 0969-806X. doi: 10.1016/j.radphyschem.2020.109080.

[106] R. Pauwels, K. Araki, J. H. Siewerdsen, and S. S. Thongvigitmanee. Technical aspects of dental CBCT: state of the art. *Dentomaxillofacial Radiology*, 44(1): 20140224, 2015. doi: 10.1259/dmfr.20140224.

[107] R. Booij, M. L. Dijkshoorn, and M. van Straten. Efficacy of a dynamic collimator for overranging dose reduction in a second- and third-generation dual

source CT scanner. *European Radiology*, 27(9):3618–3624, 2017. ISSN 0938-7994. doi: 10.1007/s00330-017-4745-8.

[108] U. Stankovic, M. van Herk, L. S. Ploeger, and J. J. Sonke. Improved image quality of cone beam CT scans for radiotherapy image guidance using fiber-interspaced antiscatter grid. *Medical Physics*, 41(6):061910, 2014. ISSN 0094-2405. doi: 10.1118/1.4875978.

[109] S. Schafer, J. W. Stayman, W. Zbijewski, C. Schmidgunst, G. Kleinszig, and J. H. Siewerdsen. Antiscatter grids in mobile C-arm cone-beam CT: effect on image quality and dose. *Medical Physics*, 39(1):153–9, 2012. ISSN 0094-2405. doi: 10.1118/1.3666947.

[110] R. Rana, A. Jain, A. Shankar, D. R. Bednarek, and S. Rudin. Scatter estimation and removal of anti-scatter grid-line artifacts from anthropomorphic head phantom images taken with a high resolution image detector. *Proc SPIE Int Soc Opt Eng*, 9783, 2016. ISSN 0277-786x. doi: 10.1117/12.2216833.

[111] P. D. Deak, O. Langner, M. Lell, and W. A. Kalender. Effects of adaptive section collimation on patient radiation dose in multisection spiral CT. *Radiology*, 252(1):140–7, 2009. ISSN 0033-8419. doi: 10.1148/radiol.2522081845.

[112] R. Ning, X. Tang, and D. Conover. X-ray scatter correction algorithm for cone beam CT imaging. *Medical Physics*, 31(5):1195–1202, 2004. ISSN 0094-2405. doi: 10.1118/1.1711475.

[113] C. Morel. Introduction to GATE, 2004. URL https://opengate.readthedocs.io/en/latest/introduction.html. Accessed on 26-12-2022.

[114] G. Poludniowski, G. Landry, F. DeBlois, P. M. Evans, and F. Verhaegen. SpekCalc: a program to calculate photon spectra from tungsten anode x-ray tubes. *Phys Med Biol*, 54(19):433–438, 2009. ISSN 0031-9155. doi: 10.1088/0031-9155/54/19/n01.

[115] G. Muehllehner. Effect of resolution improvement on required count density in ECT imaging: a computer simulation. *Physics in Medicine and Biology*, 30(2):163–173, 1985. ISSN 0031-9155 (Print) 0031-9155. doi: 10.1088/0031-9155/30/2/005.